Pleistocene aridification of the Eastern Taurides, Turkey revealed by (U-Th)/He ages of supergene mineralisation in Attepe iron deposits.

David Currie[1], Finlay M. Stuart[1], and Serdar Keskin[2]

[1]Scottish Universities Environmental Research Centre
[2]General Directorate of Mineral Research and Exploration (MTA)

November 22, 2022

Abstract

The Taurus Mountains form the southern margin of the Central Anatolian Plateau of Turkey and form an orographic barrier separating the cold, semi-arid interior to the north from the mild Mediterranean coast to the south. When and how they formed, and the extent which they have influenced the regional climate remains poorly constrained. The Attepe iron deposits sit on the northern part of the Eastern Taurus mountains at altitude of 1.5-2 km and consequently are ideally located to record interactions between climate and tectonics. (U-Th)/He ages of iron-oxide-oxyhydroxides from four mines within the Attepe iron deposits record ages of 1-5 Ma consistent with the persistence of hot humid climate conditions throughout the Pliocene and Pleistocene. In mines where samples are measured from different depths the age data are consistent with water table lowering rate of between 12.3 to 6.4 m/Myr. Translating these to rock uplift rates they are close to uplift/incision recorded within the Central Anatolian Plateau over the past 2 Ma, suggesting that the region was already at or close to its current elevation by the late Miocene. The latest goethite precipitation constrains the cessation of hot-humid climate to sometime in the last million years and implies that regional climate cooling, rather than surface uplift, was the main driver of aridification.

Pleistocene aridification of the Eastern Taurides, Turkey revealed by (U-Th)/He ages of supergene mineralisation in Attepe iron deposits.

D. Currie[1], S. Keskin[2] and F. M. Stuart[1]

[1] Isotope Geosciences, Scottish Universities Environmental Research Centre, Rankine Avenue, East Kilbride G75 0QF, UK.

[2] General Directorate of Mineral Research and Exploration, Eastern Black Sea District Office, Trabzon, Turkey.

Corresponding author: David Currie (d.currie.1@research.gla.ac.uk)

Key Points:

- Supergene Fe-oxide-oxyhydroxide from the Eastern Taurides mountains reveal (U-Th)/He ages between 1 and 5 Ma.
- Implied rock uplift rates (6 and 12 m/Ma) are low suggesting that the region was at or near the current elevation by 5 Ma.
- Aridification occurred in the last million years likely driven by regional climate cooling rather than tectonic uplift.

Abstract

The Taurus Mountains form the southern margin of the Central Anatolian Plateau of Turkey and form an orographic barrier separating the cold, semi-arid interior to the north from the mild Mediterranean coast to the south. When and how they formed, and the extent which they have influenced the regional climate remains poorly constrained. The Attepe iron deposits sit on the northern part of the Eastern Taurus mountains at altitude of 1.5-2 km and consequently are ideally located to record interactions between climate and tectonics. (U-Th)/He ages of iron-oxide-oxyhydroxides from four mines within the Attepe iron deposits record ages of 1-5 Ma consistent with the persistence of hot humid climate conditions throughout the Pliocene and Pleistocene. In mines where samples are measured from different depths the age data are consistent with water table lowering rate of between 12.3 to 6.4 m/Myr. Translating these to rock uplift rates they are close to uplift/incision recorded within the Central Anatolian Plateau over the past 2 Ma, suggesting that the region was already at or close to its current elevation by the late Miocene. The latest goethite precipitation constrains the cessation of hot-humid climate to sometime in the last million years and implies that regional climate cooling, rather than surface uplift, was the main driver of aridification.

1. Introduction

The uplift of high elevation regions such as the Tibetan Plateau and Altiplano-Puna has driven changes in regional and global climate (Molnar et al., 1993; Molnar, 2005; Allmendinger et al. 1997, Ehlers & Poulsen 2009). The Central Anatolian plateau (CAP) is a western expression of the Himalayan-Tibetan orogen to the east (Hatzfeld & Molnar 2010) and covers approximately 120,000 km^2 at an average elevation of around 1 km above sea level (Çiner et al. 2015). It is fringed to the north by the Pontid mountains and to the south by the Taurus mountains (Fig. 1). The Taurides have an average elevation of 2.4 km and act as an orographic barrier to precipitation separating the semi-arid CAP (Schemmel et al. 2013) from the mild Mediterranean climate to the south (Sensoy, 2004). The paucity of terrestrial climate records makes it difficult to determine accurately when the current semi-arid climate became established across the southern margin of the Central Anatolian Plateau (smCAP), and how it relates to the uplift of the Tauride mountains. Consequently, the timing of uplift of the Taurides and its influence on regional climate, especially in the aridification of the CAP, is contentious.

Stable isotope records of lacustrine carbonates record a relatively humid climate in the Mut Basin/Ecemis Corridor regions of the CAP from the late Oligocene to early Miocene (Ludecke et al., 2013). While by the early Miocene the CAP was yet to be fringed by orographic barriers to the north and south, the depositional environment had shifted from large, open freshwater to smaller closed saline lakes despite high humidity climate (Ludecke et al., 2013). The lack of significant pre-Miocene orographic rain-out has been recognised in the $\delta^{18}O$ composition of carbonates from large continental basins, although the data point to the onset of uplift and establishment of an orographic barrier by 5 Ma (Ludecke et al., 2013; Meijers et al., 2016; 2018). Throughout the late Miocene the smCAP drained internally, however by the early Pliocene it was connected to the Mediterranean Sea (Meijers et al., 2020). In the eastern Mediterranean, underplating of material derived from the African plate during progressive collision with the Anatolian plate led to Late Messinian uplift of marine sediments in the Adana basins, south of the Taurides, establishing drainage to the Mediterranean Sea and resulting in the deep incision of the Taurides (Jaffey & Robertson 2005). The initiation of uplift across the smCAP from late Miocene times may reflect lithospheric slab break-off and upwelling of mantle asthenosphere, and perhaps the arrival of the Eratosthenes Seamount at the collision zone south of Cyprus (Cosentino et al. 2012, Schildgen et al., 2012, Schildgen et al., 2014, Radeff, 2014).

Meijers et al. (2020) proposed that a sub-humid Anatolian climate persisted during late Miocene surface uplift, and that the smCAP had a relatively low relief during CAP uplift with stable (>1 Ma) palaeoenvironmental and hydrological conditions based on the stable isotope composition of lacustrine carbonates. Delayed aridification of the CAP and its southern margin was potentially caused by an increase in mean annual precipitation into the Pliocene (Kayseri-Özer 2017). The Quaternary marine terraces along the smCAP allowed Racano et al. (2020) to develop a landscape evolution model that suggested the mountain belt was essentially formed during a pulse of rapid uplift (1.9 to 3.5 m/kyr) between 500 and 200 kyr that resulted in 1.5-2 km of surface uplift (Racano et al., 2020). This is supported by the occurrence of middle Pleistocene benthic fauna, indicative of an epibathyal marine environment, now identified along the smCAP on a palaeocoastline at ~1500 m above sea level to suggest a short-lived pulse of rapid uplift (3.2-3.4 m/kyr) since the middle Pleistocene (~450 kyr) (Öğretmen et al., 2018). This requires that the modern topography and the orographic barrier along the smCAP was established in the last 500 kyr.

Fe-oxides-oxyhydroxides (Fe-O) are ubiquitous near surface weathering products formed in relatively wet humid climates (e.g. Tardy and Nahon, 1985; Vasconcelos et al., 2015). Age determinations of supergene minerals within weathering profiles are now widely used to provide constraints on the timing of climate and tectonic processes that control chemical weathering rates (e.g., Vasconcelos, 1999; Beauvais et al., 2016; Deng et al., 2017). The modest U and Th content of Fe-O minerals results in the generation of significant and measurable amounts of ^{4}He by radioactive decay. At surface temperatures the diffusion rate of He within Fe-O minerals is low enough that it is quantitatively retained and the (U-Th)/He ages can be used to determine the timing of mineral precipitation (e.g. Schuster et al., 2005; Danisik et al., 2013). Consequently Fe-O He ages are now widely used to determine when climate conditions were conducive to supergene mineralisation (Vasconcelos et al., 2015), and they have proved useful for constraining how and when tectonic uplift initiate a change in climate, for example, the onset of aridity in the Central Andes (Cooper et al. 2016) and changes to Asian monsoon dynamics (Deng et al. 2017).

The Attepe iron deposits are located at 1.5-2 km above sea-level on the northernmost fringe of western extremity of the Eastern Taurus mountains and are ideally located to track the climate and uplift history of the smCAP (Figure 1). Over 90% of the iron production and exploration is concentrated in 20-50 m thick oxidised zones in the upper part of all deposits (Kupeli, 2010; Keskin and Ünlü, 2016). The current cold, semi-arid climate of the region is not conducive to supergene oxidation. Consequently, dating the supergene alteration of the deposits has the potential to constrain the timing of climate change in the Taurides and how this relates to mountain belt evolution. Here we present (U-Th)/He ages of fully-characterised supergene Fe-O mineralisation from four mines within the Attepe district in order to determine when climate conditions on the smCAP were conducive to supergene enrichment and when the current cold semi-arid climate was established.

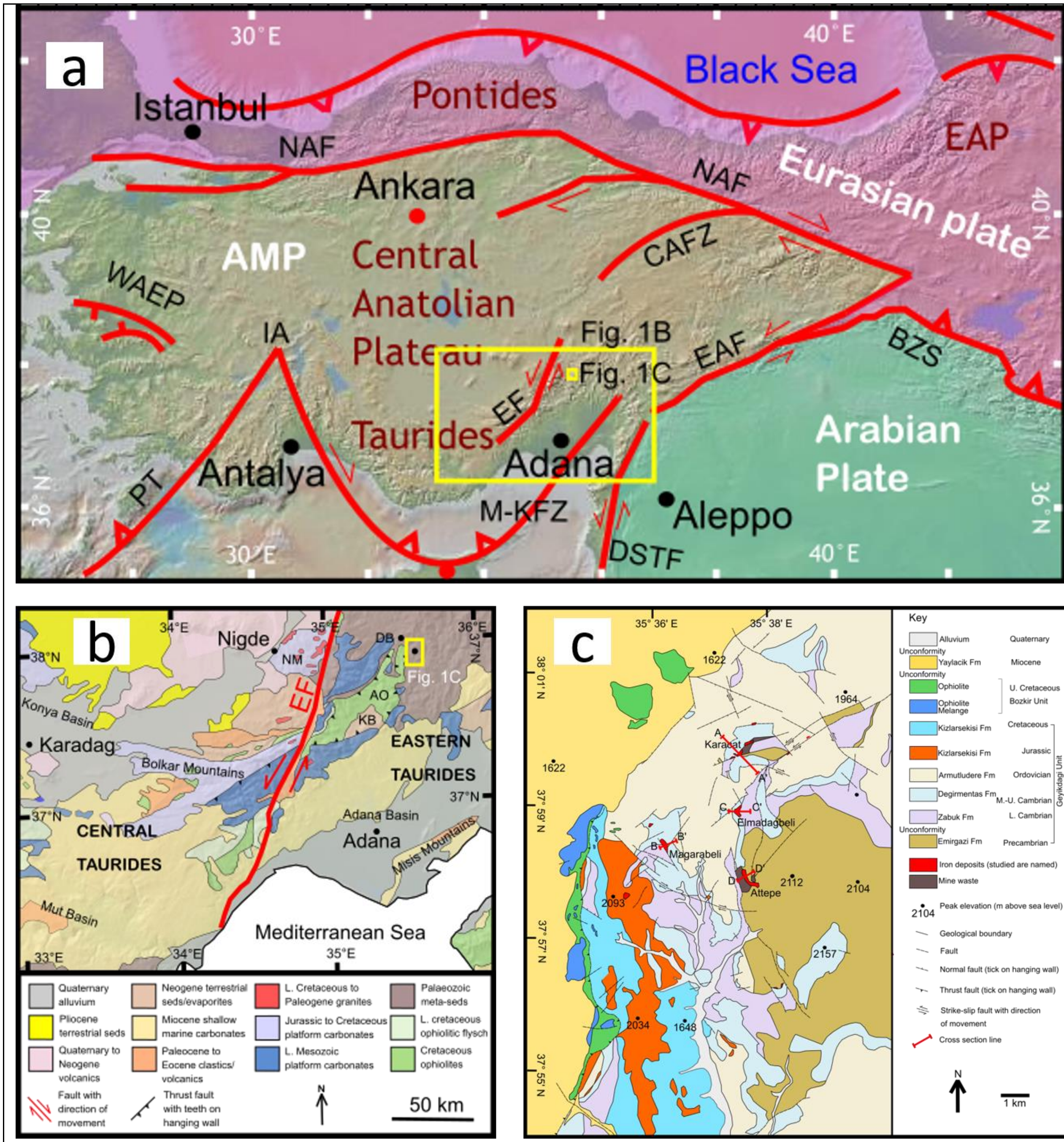

Figure 1: a) Large-scale map of Greater Anatolia showing major faults and tectonic plate arrangement adapted from Dilek and Sandvol (2009) and Walsh-Kennedy et al. (2014). b) Regional geology of the central southern margin of the Central Anatolian Plateau (smCAP) adapted from Dilek and Sandvol (2009). c) Geological map of the Attepe iron deposits adapted from Keskin (2016). Formation descriptions in stratigraphic column (Supplimentary Information: Fig. S6). AO – Aladag ophiolite, KB – Karsanti Basin, DK – Dikme Basin, NM – Nigde Massif, EAP – East Anatolian Plateau, AMP – Anatolian microplate, NAF- North Anatolian fault, CAFZ – Central Anatolian fault zone, WAEP – Western Anatolian extensional province, IA – Isparta Angle, PT – Pliny trench,M-KFZ – Misis-Kyrenia Fault Zone, EF – Ecemis fault zone, EAF –

East Anatolian fault, DSTF – Dead Sea transform fault, BZS – Bitlis-Zagros suture. Panel a and b background from GeoMapApp (Ryan et al., 2009).

2. Geological Setting

The Taurus Mountain chain runs for over 1,500 km across southern Turkey to Iran. They record a complete plate-tectonic cycle beginning with Palaeoozoic rifting, followed by seafloor spreading, and final collision of African and Eurasian plates during the late Mesozoic to early Cenozoic (Robertson et al., 2007). They are widely interpreted to be composed of continental fragments rifted from North Africa during the Mesozoic opening of the Southern Neotethys Ocean (Şengör and Yilmaz 1981; Robertson & Dixon 1984). The progressive closure of the Southern Neotethys Ocean is associated with ophiolite emplacement during the late Cretaceous and ultimately closure by the Miocene (Robertson et al., 2007). Further convergence resulted in the westward escape of the Anatolian microplate along the Northern and Eastern Anatolian fault zones from the mid-Miocene (Sengor, 1985; Bozkurt, 2001). This movement continues today as Anatolia undergoes counter-clockwise rotation and westward escape from Eastern Anatolia at a rate of ~30 mm/yr (Bozkurt, 2000). The Tauride Mountains are typically divided into Western, Central, and Eastern Taurides, with the latter found east of the Ecemis Fault and of primary interest to this study.

Middle to late Miocene marine fossil assemblages in the Dikme basin, ~10 km north west of the Attepe district, records the final marine incursion into the smCAP (Ocakoglu, 2002). To the south-west, 6.7 Ma marine sediments of the Mut-Ermenek Basin are now at 1.5-2 km implying that surface uplift rates of 200-300 m/Myr (Cosentino et al., 2012; Schildgen et al., 2012). This may have been initiated by the switch from crustal shortening to extension along the smCAP, linked to oceanic slab break off and tearing in middle to late Miocene (Schildgen et al., 2014). Cosmogenic nuclide surface exposure ages of strath terraces in the Mut basin reveal average uplift rates of 250 to 370 m/Myr since 8 Ma with periods of higher uplift rate of between 600 to 700 m/Myr after 1.66 Ma (Schildgen et al., 2012). From early to middle Pleistocene, this increase in uplift across southern Turkey may be the result of collision between the Eratosthenes Seamount and the subduction trench where African and Eurasian plates converge to the south of Cyprus (Schildgen et al., 2012).

The Attepe mining district is between 1.5 and 2 km above sea level on the western side of the Eastern Taurus Mountains in the Kayseri-Adana region of southern Turkey (Fig. 1) (Küpeli 2010). It is one of Turkey's most important Fe-ore producers, with proven reserves of up to 70 Mt and an estimated 1 Mt of ore currently extracted annually from the Attepe and Elmadagbeli mines at average grade of 45-58 % Fe_2O_3 (Kupeli, 2010; Keskin, 2016). The main ore hosting formations are present within the metasedimentary rocks of the 4 km thick Palaeozoic Geyikdagi Unit (Supplimentary Information: Fig. S1-S4). Basement lithologies have been subject to low grade metamorphism with multiphase deformation superimposed during Caledonian, Hercynian and Alpine orogenic events (Küpeli 2010; Keskin, 2016).

The oldest mineralisation phase is an uneconomic syn-sedimentary pyrite and hematite hosted in Precambrian Emirgazi formation metasedimentary and metavolcanic units (Küpeli 2010). A later phase of Paleocene to Lower Eocene hydrothermal-metasomatic vein-type iron carbonate mineralisation is hosted in middle to upper Cambrian Degirmentas formation dolomitic limestones. The ore bodies occur as veins, lenses or stocks composed ankerite and siderite with associated hematite, chalcopyrite, tetrahedrite, pyrite and marcasite veins hosted in the Emirgazi, Cambrian Degirmentas and Armutludere, and Jurassic Kizlarsekisi formations (Kupeli, 2010; Keskin, 2016). The mineralisation is controlled by NE-SW and ENE-WSW trending fault systems which provided pathways for hydrothermal fluid flow. The most economic deposits occur where the fault systems intersect (Kupeli, 2010; Keskin and Ünlü, 2016).

The hydrothermal-metasomatic mineralisation has been subjected to extensive supergene alteration, termed karstic Fe-oxi-hydroxide (KIO) mineralisation by Kupeli et al. (2007). Weathering profiles are present at all mines, evident from the 20-80 m thick zones of dominantly limonite, goethite, and hematite, with less abundant malachite, azurite, lepidocrocite, manganite and calcite. The uppermost part of the supergene zones have been removed in many cases. The oxidation zones in each mine are not laterally consistent within the deposits, they tend to replace the vein-type ores along faults and fracture systems (Supplementary Information: Figures S1-S4). In the field the oxidation zones are recognised as intensely weathered friable rock, boxwork textures, and occurrences of botryoidal goethite (Figs. S1-S5). The oxidation phase is the dominant source of iron ore in the district, accounting for more than 90% of the extracted iron (Küpeli 2010). The Attepe mine is the largest and most economically important of the deposits, approximately 500 x 500 m and in places up to 200 m deep (Supplimentary Information: Fig. S7) (Küpeli 2010; Keskin, 2016).

The climate of the region is classed as semi-arid; mean summer temperatures are 23°C, mean winter are typically -2°C and annual precipitation never exceeds 500 mm (Schemmel et al., 2013). The town of Niğde ~80 km west of the Attepe district at ~1300 m above sea level has a cold semi-arid climate, with hot dry summers (mean temperature 20°C) cold and often snowy winters (mean 4.3°C) and 90% of the precipitation (<350 mm) falling between autumn and spring (Sarikaya et al., 2015). To the south of the smCAP a mild Mediterranean climate prevails where mean annual rainfall exceeds 1000 mm (Sensoy, 2004). Topography immediately to the north of the Attepe iron deposits becomes less mountainous and merges with the CAP, whereas to the south it becomes mountainous with steep river valleys and defined peaks > 2 km. The Zamanti River drains the region and runs from the north near Kayseri, south past Dikme ~10 km to the NW of Attepe iron deposits and through the Taurides before joining the Göksu River and forming the Seyhan River, the largest river draining to the Mediterannean, ~ 80 km to the north of Adana.

3. Samples

We have analysed seven Fe-O samples from four mines; Attepe, Magarabeli, Karacat, and Emladagbeli (Table 1). In-situ samples were taken from the weathering sections near the diffuse base of the supergene zone of the active mine workings (Figures S1-S4). All samples were taken from veins or cavity and fracture infills. Areas of high purity were selected to minimise contamination by hypogene phases. The purity, composition, and crystal morphology of all samples were investigated by X-ray diffraction analyses and scanning electron microscopy. From the XRD spectra samples S1, S3, and S11 are pure goethite, S4 and S8 are hematite-goethite mixtures, S9 is a mixture of hematite with minor magnetite (Fe_3O_4) and S10 is hematite only (Supplementary Information: Table S1; Fig. S8). No minor phases were present above detection limit (<1%) (Fig. S8). All samples are poly-crystalline, showing boxwork texture indicative of supergene weathering with many crystal forms (e.g. botryoidal, prismatic, needle-like, fibrous or platy) (Fig. 2). Colloform banding provides evidence of mineral precipitation from a fluid phase into open spaces (Fig. 2). Crystal dimensions range from 0.1 μm to 300 μm and typically make up larger aggregates of crystals or form ribs in the pervasive boxwork texture.

The average crystallite size (or mean coherent domain size) for each sample was obtained by applying the Scherrer equation to each sample x-ray diffractogram result (Table S1). Average crystallite sizes range from 28 ± 10 nm to 84 ± 2 nm. The pure goethite samples tend to record greater average crystallite size, though not entirely (Fig. S9). Crystallite size is generally taken as the cube root of the volume of a crystallite and, using the Scherrer equation to calculate it, provides a lower estimate of crystallite size since the effects of strain and crystal lattice imperfections on peak width are not considered (Speakman, 2014). Further, if sample material has average crystallite size <100 nm it is taken as the thickness of the crystallite analysed (Monshi et al., 2012). Crystallite size is not necessarily grain size, since grains can be composed of many crystallites (Monshi et al., 2014). This method for crystallite size estimation allows for the correction of diffusive loss of He from Fe-O, like in Allard et al. (2018). However, Allard et al. (2018) use Rietveld refinement prior to calculation of crystallite size which accounts for strain and crystal lattice imperfection.

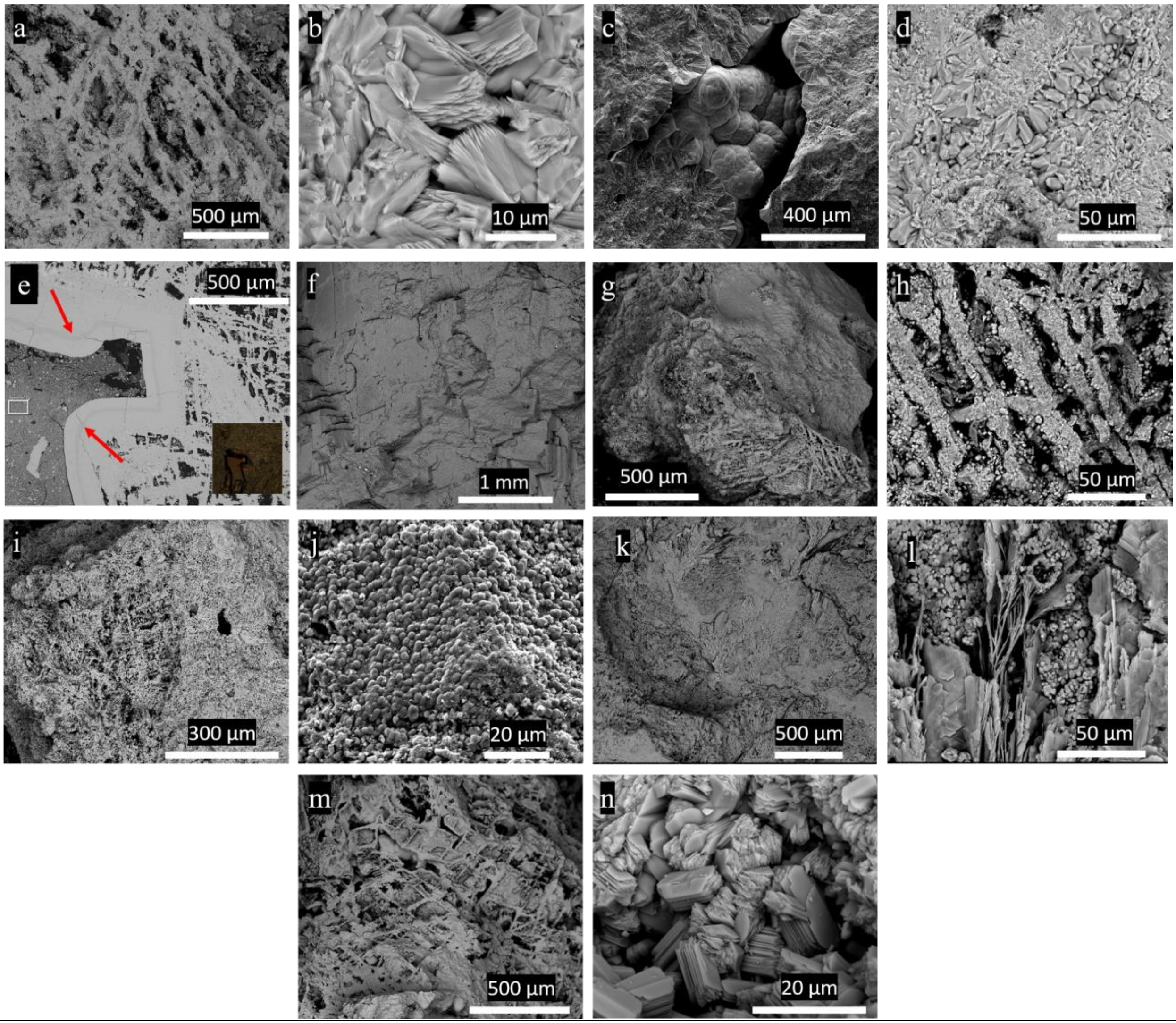

Figure 2: Back-scattered electron SEM images of supergene iron oxyhydroxide textures from the Attepe iron ore deposits. a) S1: Boxwork texture with protruding ribs and hollowed central section. B) S1: Plate-like morphology of goethite crystals within rib of boxwork texture. c) S3: Botryoidal goethite filling open-space. d) S3: Poly-crystalline goethite with prismatic, needle-like, and platy crystal morphology. Boxwork ribbing is typically composed of plate-like and prismatic morphology whereas hollowed central sections are primarily filled with needle-like goethite. e) S3: BSE image of image showing colloform texture of goethite filling open/partially filled space. Boxwork texture on the inner surface of colloform banding (top, right, and bottom right of image) This implies that final boxwork development is synchronous with colloform banding. f) S4: BSE image showing blocky, cubic fracturing of sample chip. g) S8: Fractured chip highlighting pervasive boxwork texture. h) S8: Boxwork texture with fibrous masses of hematite and goethite coating the outer surface of ribs and growing into open spaces. i) S9: Chip exhibiting boxwork texture and multiple open spaces. j) S9: Reniform masses of hematite coating a surface on the sample. k) S10: Boxwork and dendritic textures in hematite. l) S10: High magnification image of dendritic platy hematite alongside reniform balls of hematite. m) S11: Boxwork texture in goethite. n) S11: Plates of goethite which form the ribs of boxwork

texture.

4. Analytical Procedures

Samples were dried, gently crushed and 1-2 mm chips free of gangue minerals were picked, crushed and sieved. Gangue minerals, predominantly calcite and quartz, were removed from the 0.25-1 mm fraction using a Frantz LB-1 magnetic separator and hand-picking under binocular microscope. This fraction was re-crushed and gangue minerals removed from the 150-250 μm fraction. A final crush step using a quartz-agate pestle and mortar was used to produce a <38 μm fraction for powder X-ray diffraction (XRD), and He, U and Th determinations. XRD was carried out using a Panalytical X'Pert PRO MPD (A3-26) at School of Chemistry, University of Glasgow. The diffractometer is equipped with a Cu target tube operated at 40 kV and 40 mA and was set to scan between 10 and 60° 2θ scan range with a step size of 0.017° with each step taking between 60-150 seconds. Small rock chips were imaged using a FEI Quanta 200F environmental scanning electron microscopy (SEM) operated at 20 kV at the ISAAC facility at University of Glasgow (Lee et al., 2014).

Analytical procedures for He dating were similar to those of Wu et al. (2019). In order to avoid problems associated with the volatilisation of U and Th during the heating (800-1000°C) required for He extraction (e.g. Vasconcelos et al. 2013; Danisik et al., 2013; Hofmann et al. 2020) we have determined He separately from U and Th in multiple aliquots of several mg of each sample. This data was used to calculate an average He concentration and average U and Th concentration for each sample, which were used to determine the sample (U-Th)/He age using the formulation of Meesters and Dunai (2005). This procedure has been used successfully to date hematite mineralisation from Elba yielding ages that are indistinguishable from Ar/Ar ages of cogenetic adularia (Wu et al. 2019). The technique differs from the standard technique where multiple single aliquots are dated, which often yields over-dispersed age populations (e.g. Cooper et al. 2016; Danisik et al., 2013; dos Santos Albuquerque et al., 2020).

Helium concentrations were determined in 6-9 aliquots of each sample. Between 3 and 9 mg of <38 μm fraction were weighed into Pt-foil packets. Typically, four sample aliquots and one empty packet were placed 10 mm apart in recesses in a degassed Cu pan and covered with a sapphire window prior to overnight pumping at 80°C to minimise background levels of H and CH_4. Helium was extracted by heating the Pt packets to 1000 ± 20°C for 300 seconds using a 960 nm diode laser heating system (Fusions 960, Photon Machines). Laser power was regulated using the inbuilt pyrometer which maintained sample temperature. All sample tubes were re-heated to ensure complete He extraction. Sample re-heats released on average 0.2% of the initial He and were not used in He concentration determinations. The evolved gases were purified for 600 seconds using a combination of hot and cold SAES TiZr getters and two liquid nitrogen-cooled charcoal traps. Helium abundances were determined using a Hiden HAL3F quadrupole mass spectrometer operated in static mode (Foeken et al. 2006). Absolute ^{4}He concentrations in samples were calculated by peak height comparison against repeated measurements of a calibrated He standard. Blocks of standard determinations were carried out before and after every two sample aliquots. Within these distinct analytical periods He sensitivity varied by ±1%. Helium blanks (3.6×10^{-11} ccSTP ± 73 %, n = 62) were determined by heating empty Pt tubes. Sample He contents were always more than 100 times the blank values.

Uranium and thorium concentrations were determined on 3-5 aliquots of 2-5 mg Fe-O. The sample dissolution procedures were essentially identical to those developed by Wu et al. (2019). U and Th were measured in Agilent 7500ce Q-ICP-MS. Blank levels were between 0.06 ± 0.05 ppm for U and 0.11 ± 0.10 ppm for Th. U and Th analysed in four aliquots of hematite (Italy-4) from the Rio Marina mine Elba yielded ^{238}U and ^{232}Th concentrations that overlapped values determined by in Wu et al. (2019) (Table 1).

5. Results

^{4}He concentrations range from 0.49 to 8.3 x 10^{-10} ccSTP/mg (Table 1). Weighing error, blank corrections and mass spectrometer sensitivity variation means that individual He concentration determinations have an uncertainty of ±2 %. This is less than the range of He concentrations measured of multiple aliquots of each samples (±4-7 %). ^{238}U concentrations range from 0.07 to 1.55 ppm. Th was only measurable in four of the seven samples, ranging from 0.01 to 0.19 ppm. Th/U ratios in the four Th-bearing samples vary from 0.16-2.43 but tend to be consistent within sample. Single U and Th concentration determinations typically have an uncertainty of ±2 %. The within-sample effective uranium content (eU = [U] + 0.235 x [Th]) is ± 5 % in all but one sample.

Average (U-Th)/He ages for each sample calculated using the mean He and eU concentrations range from 0.90 to 5.08 Ma (Table 1). No alpha ejection correction was applied, consistent with other studies of Fe-O (e.g. Shuster et al., 2005; Vasconcelos et al., 2013; Allard et al., 2018; dos Santos Albuquerque et al., 2020). The total uncertainty of the average He ages is ±5-18 % (1σ).

Table 1: Sample information and (U-Th)/He data for Fe-O samples from the Attepe iron deposits, Turkey.

Sample	Mineralogy	Deposit	Elevation (m)	Mean Crystallite Size (nm)	Aliquot	Mass (mg)	^{4}He (ccSTP/mg)(10^{-10})	Mean ^{4}He (ccSTP/mg) (10^{-10})	Aliquot	Mass (mg)	^{238}U (ppm)	±	^{232}Th (ppm)	±	Th/U	eU	He Age (Ma)	±	Corrected Age (Ma) (Do=10)	±
S1	Goethite	Attepe	1796	72	1.1	4.3	1.09	1.15 ± 0.04	1.7	2.2	0.38	0.01	0.12	0.01	0.32	0.41	2.27	0.12	2.32	0.13
					1.2	4.4	1.10		1.8	2.4	0.48	0.02	0.11	0.01	0.23	0.51				
					1.4	4.9	1.18		1.9	1.8	0.39	0.01	0.11	0.01	0.28	0.42				
					1.6	5.0	1.17		1.10	2.2	0.36	0.01	0.10	0.01	0.28	0.38				
					1.7	4.9	1.22		1.11	5.1	0.42	0.01	0.14	0.01	0.33	0.45				
					1.8	5.0	1.15													
					1.9	4.5	1.15													
S3	Goethite	Attepe	1811	66	3.10	5.4	7.33	7.48 ± 0.50	3.1	5.1	1.28	0.14	*			1.28	4.54	0.59	4.68	0.61
					3.11	4.5	7.20		3.2	5.3	1.46	0.14				1.48				
					3.12	6.0	6.47		3.3	4.8	1.30	0.15				1.31				
					3.16	4.0	7.40		3.4	4.9	1.29	0.15				1.30				
					3.17	3.6	7.31		3.5	4.7	1.39	0.16				1.40				
					3.18	5.6	8.26													
					3.19	5.9	7.61													
					3.20	5.4	7.84													
					3.21	5.4	7.84													
S9	Hematite/Magnetite	Magarabeli	1542	40	9.7	4.5	3.37	3.30 ± 0.23	9A	4.3	1.01	0.01	*			1.02	2.86	0.32	2.97	0.34
					9.8	3.3	3.33		9B	3.9	0.90	0.01				0.90				
					9.9	6.2	3.32		9C	4.1	0.91	0.01				0.91				
					9.10	5.3	2.91		9D	4.1	0.97	0.01				0.97				
					9.11	5.3	3.01													
					9.12	5.5	3.38													
					9.13	4.8	3.51													
					9.14	5.6	3.57													
S8	Hematite/Goethite	Magarabeli	1550	28	8.10	9.1	5.98	5.79 ± 0.32	8.1	5.3	1.46	0.14	*			1.46	3.21	0.36	3.4	0.38
					8.11	5.4	5.85		8.2	5.0	1.55	0.15				1.56				
					8.12	5.5	5.56		8.3	5.1	1.49	0.14				1.50				
					8.14	4.0	5.27		8.4	4.8	1.43	0.15				1.44				
					8.15	4.4	5.49		8.5	5.1	1.43	0.14				1.44				
					8.16	5.1	5.89													
					8.17	5.4	6.10													
					8.18	6.5	6.21													
S4	Hematite/Goethite	Elmadagbeli	1954	28	4.1	5.0	0.59	0.52 ± 0.04	4.7	2.000	0.43	0.01	0.07	0.01	0.16	0.45	0.90	0.14	0.95	0.15
					4.2	6.4	0.50		4.8	1.9	0.46	0.02	0.07	0.01	0.16	0.48				
					4.3	4.7	0.50		4.9	1.9	0.47	0.02	0.11	0.01	0.23	0.50				
					4.4	4.2	0.52													
					4.6	5.2	0.49													
					4.8	5.7	0.52													
S11	Goethite	Elmadagbeli	2002	84	11.1	5.4	0.86	0.92 ± 0.06	11A	4.1	0.11	0.02	0.19	0.01	1.73	0.15	5.08	0.93	5.18	0.95
					11.2	5.9	0.90		11B	4.3	0.10	0.02	0.19	0.01	1.90	0.14				
					11.3	5.6	0.91		11C	4.1	0.07	0.02	0.17	0.01	2.43	0.11				
					11.4	5.4	0.89		11D	4.2	0.09	0.02	0.18	0.01	2.00	0.13				
					11.5	5.4	0.95													
					11.6	5.0	1.02													
S10	Hematite	Karacat	1757	35	10.1	5.1	0.73	0.67 ± 0.03	10A	4.2	0.42	0.02	0.12	0.003	0.29	0.45	1.19	0.10	1.25	0.10
					10.2	4.5	0.67		10B	4.1	0.45	0.02	0.12	0.002	0.26	0.48				
					10.3	4.7	0.68		10C	3.8	0.46	0.02	0.13	0.01	0.27	0.49				
					10.4	4.8	0.63		10D	4.0	0.42	0.02	0.11	0.01	0.26	0.45				
					10.5	5.4	0.66													
					10.6	5.3	0.67													
Italy 4C	Hematite	Elba						2.76 ± 0.02 ^	A	7.90	0.30	0.01	0.43	0.01	1.44	0.40	5.60	0.23		
									B	8.10	0.31	0.01	0.42	0.01	1.35	0.41	5.58	0.20		
									C	8.47	0.32	0.00	0.40	0.01	1.23	0.42	5.43	0.10		
									D	9.13	0.32	0.00	0.41	0.01	1.27	0.41	5.48	0.10		

* Value at or below blank level
^Value from Wu et al. (2019)

6. Discussion

6.1 Post-formation He Loss

Diffusive loss of He from Fe-O can be significant at low temperatures and should be accounted for when determining mineral crystallisation ages from (U-Th)/He data (Shuster et al., 2005; Vasconcelos et al., 2013; Allard et al. 2018). Helium diffusion rates are governed by mineral chemical composition and temperature, while the proportion of radiogenic He lost from any sample is strongly dependent on mineral grain size (Farley, 2018). Where the deficit gas fraction has been determined on specific samples using the $^4He/^3He$ technique (e.g. Shuster et al., 2005; Heim et al., 2005; Deng et al., 2017), the percentage of He lost by diffusion can be constrained and corrected He age calculated. However, the parameters of He diffusion in the goethite and hematite are well established (Schuster et al., 2005; Farley 2018) and the extent of He loss can be determined, and (U-Th)/He ages reconstructed, if mineral composition and grain size is known (e.g. Allard et al. 2018).

Helium diffusion in crystalline hematite is slow at low temperature (Bahr et al. 1994; Farley et al. 2018). For example, over 90 % of He is retained in 20 nm crystallites held at 30°C for 100 Ma, comparable to the He loss rate from 100 μm diameter apatite grains (Farley 2018). Goethite is typically composed of poly-crystalline aggregates of varying properties and the more open crystal structure results in faster He diffusion. Shuster et al. (2005) showed that goethite contains regions with distinct He retention properties termed low resistivity domains (LRD) which likely account for most of the diffusive loss of ^4He. Extrapolating the data derived from $^4He/^3He$ analysis they showed that 3 to 10% of the He is lost at 25°C (Shuster et al. 2005). These distinct retention domains have been recognised in subsequent studies (Heim et al. 2006, Vasconcelos et al., 2013; Deng et al. 2017). By incorporating the crystallographic characterisations of goethite from ferruginous duricrust into the He production-diffusion code HeFTy (Ketcham 2005), Allard et al. (2018) were able to simulate He retention in spherical domains of different radii. Using the diffusion coefficients of Shuster et al. (2005) and Vasconcelos et al. (2013) they determined that 10 to 25% of He is lost from 20 nm and 13 nm diameter goethite crystallites respectively at 25°C.

The crystallite-size of the samples in this study leaves them susceptible to He loss and requires that a correction be made to the (U-Th)/He ages (Table 1). By assuming the maximum diffusion coefficient (D_o) value of 10 (Shuster et al., 2005; Vasconcelos et al., 2013), adopting the relationship between D_o and crystallite size defined by Allard et al. (2018) and using the mean crystallite size of samples determined by XRD, we can determine an upper limit on the proportion of He lost. Using this technique, we calculate that the goethite samples (S1, S3, and S11) have lost up to 6% of their He. The age correction to the mixed hematite-goethite samples (S8 and S4) has been determined based on the proportion of goethite as measured by XRD and also does not exceed 6%. Sample S10 from the Magarabeli mine is essentially pure hematite and requires an age correction of up to 4%. The diffusion-corrected ages suggest that the upper limit on the supergene mineralisation ages (0.95 ± 0.15 to 5.18 ± 0.95 Ma) are not significantly different to the uncorrected ages, and the age difference is within the analytical uncertainty (Table 1). We conservatively use the diffusion-corrected ages in the following discussion. There is no relationship between age and crystallite size, mineralogy or eU (Figures S9-10).

6.2 Implications for the climate and uplift history of the smCAP

The earliest supergene mineralization is recorded by goethite from the Elmadegbeli deposit, the highest altitude sample (2002 m), which formed at 5.18 Ma. The latest supergene phase is S4 (0.95 Ma), the lower sample from the Elmadegbeli mine (1994 m). The lowest altitude sample from the Attepe mine (S1; 1796 m) is younger than S8 from the Magarabeli mine despite it being from more than 200 m higher elevation (Fig. 3). It is likely that the water table was locally variable, and that faulting post-formation of the supergene profiles has changed the elevation of the weathering profiles relative to each other. For instance, the Ecemis Fault Zone (Fig. 1) that runs NE-SW through the smCAP has experienced ~60 km of sinistral displacement (Jaffey and Robertson, 2001). The Ecemis Fault Zone is a present-day seismic hazard and is one of Turkey's most prominent fault zones (Yildirim et al., 2016). Movement on the Civizlik Fault, ~60 km WSW of the Attepe iron deposits, has caused 13 m of vertical offset in moraine and talus fan surfaces in the last 22 ka, while the adjacent Kartal Fault records 120 m of vertical offset in the past 104 ka (Yildirim et al., 2016).

The earliest He age recorded in this study (5.18 ± 0.95 Ma) are consisten with Late Miocene pollen records for the Kersihir-Kizilok region, 200 km northwest of the study area, that reveal climate conditions were conducive for supergene Fe-O enrichment; mean annual temperature of 17°C and precipitation of 1045 mm (Kayseri-Özer, 2017). The persistence of similar climate regime into the early Pliocene has been documented across Central and Eastern Anatolia (Kayseri-Özer 2017). Evidence of earlier supergene Fe-O mineralisation in the region awaits a more detailed investigation.

The Attepe iron deposits lie on the northern edge of the smCAP. It is likely that they were already at significant elevation by the late Miocene (Schildgen et al., 2012; Cosentino et al., 2012; Schildgen et al., 2014; Radeff, 2014) with an emergent orographic barrier in close proximity (Ludecke et al., 2013; Meijers et al., 2016; Meijers et al., 2018). For instance, the early Miocene Dikme basin, approximately 15 km to the northwest of the Attepe district, has been above sea level since 14 Ma (Ocakoglu, 2002) and was likely at ~1.8 km elevation by 5 Ma (Meijers et al., 2018). Uplift relative to base level would have caused drainage reorganisation (Jaffey & Robertson 2005; Meijers et al., 2020) and driven the generation of weathering profiles if local water table reduced relative to land surface so long as the climate was conducive to supergene enrichment.

The Fe-O age data are difficult to reconcile with the model of rapid rock uplift resulting in the Attepe region reaching its current elevation in the past 500 ka (Öğretmen et al. 2018; Racano et al. 2020). This would have generated significantly younger He ages as the absence of an orographic barrier until 500 ka would have allowed hot-humid climate to have persisted across the region, resulting in continued precipitation of supergene minerals into the middle Pleistocene. The youngest ages of 1.25 ± 0.10 Ma and 0.95 ± 0.15 Ma do not reflect this.

In the three mines where two samples were analysed (Elmadegbeli, Attepe, and Magarabeli) there is a systematic age increase with elevation (Fig. 3). Such age-depth relationships are typical of supergene profiles and are widely held to reflect the downward migration of a weathering front related to lowering of the local water table (e.g. Vasconcelos 1999; Cooper et al. 2016; Deng et al. 2017). In a climate conducive to supergene enrichment, rock uplift and consequent river channel incision lower the water table, resulting in mineral precipitation ages that decrease with depth in a weathering profile (e.g. Deng et al. 2017). The elevation-age relationships at Attepe and Elmadagbeli mines record average incision rates of induced lowering of the water table relative to the land surface of 12.3 and 6.4 m/Myr between 5 and 1 Ma and 2.2 and 4.8 Ma respectively (Fig. 3). Such low incision/rock uplift rates are broadly consistent with the low rate determined for the CAP on the basis of river incision over the last few Myrs (Doğan, 2011) and supports the prevailing view that the Eastern Taurides must have been at or close to current elevation prior to 5 Ma. The preservation of the thin carapace of weathered rock on the Attepe deposits is difficult to reconcile with the majority of the 1-2 km of uplift required for the current elevation to have occurred in the last million years.

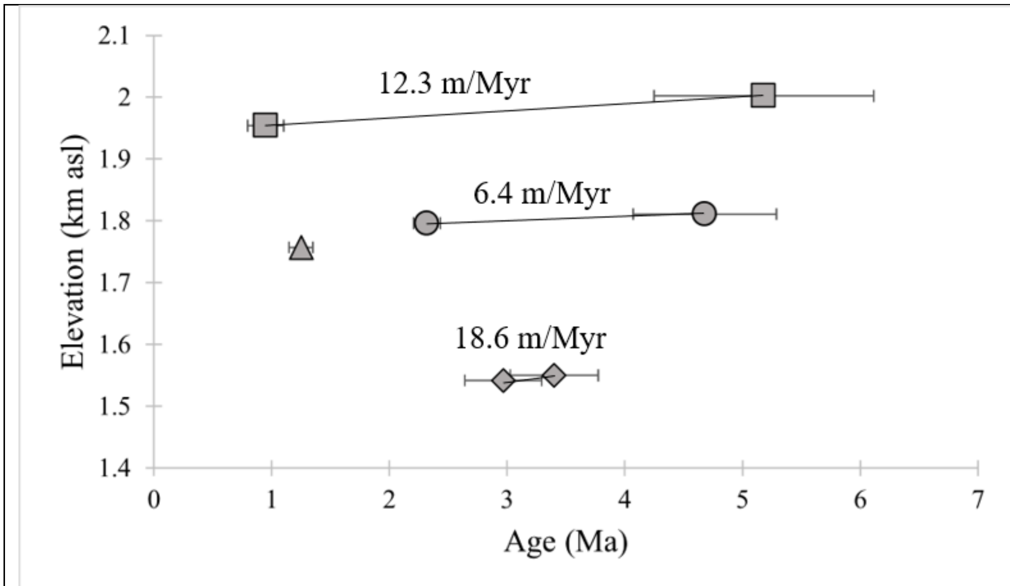

Figure 3: Age versus elevation plot of Attepe iron deposit samples with uplift/incision rates for each pair given above. Square = Elmadagbeli mine. Circle = Attepe mine. Diamond = Magarabel mine. Circle = Karacat mine.

The youngest supergene He ages (1.25 ± 0.10 Ma and 0.95 ± 0.15 Ma) from samples from near the base of the Karacat and Elmadagbeli mines record the latest supergene enrichment. They require that hot-humid climatic conditions across the region persisted into the Middle Pleistocene, and imply that the current cooler and drier climate regime was established sometime in the last million years or so. This contrasts starkly with the prevailing view which considers that the onset of aridification across the CAP began by the middle Pliocene due to uplift and reorganisation of drainage (Meijers et al., 2020). It is, however, consistent with $\delta^{13}C$ and fauna data from pedogenic carbonates and calcretes in the Cal Basin which record a shift from Pliocene sub-humid to Pleistocene arid climate (Alçiçek and Alçiçek, 2014). Soil stratigraphy and the occurrence of palygorskite and kaolinite in the Adana basin, ~150 km south of Attepe, indicate that the wet to dry climate transition occurred during the Pleistocene (Kapur et al., 1993). Further study revealed mean annual temperatures in the northern portion of the Adana basin to be 21-23°C with the presence of palygorskite and tree, shrub, and grass vegetation suggesting a semi-arid climate between 782 and 250 ka (Kaplan et al., 2013). Using calcrete formations, Eren et al. (2008) propose that semi-arid climate was establisged in the northern Adana Basin between 782 ka and 250 ka. They suggest a mean annual temperature of ~18°C and mean annual precipitation of <300 mm/yr; similar in temperature yet more arid than that of today in that region (>600 mm/yr) (Eren et al., 2008). Alluvial fan deposits in the high elevation (>2 km) Ecemis River drainage area, ~60 km to the west of the Attepe region, record major climate shifts between cooler glacial periods and warmer interglacial/interstadial conditions from ~136 ka until the Pleistocene-Holocene transition (Sarikaya et al., 2015).

Continuous long-term terrestrial climate records of Eastern Mediterranean and Western Asia are sparse. By interpreting European Cenozoic cool-temperature tree flora, Svenning (2003) showed that the vegetation widespread today are those most tolerant of a cold growing season whilst those in the Mediterranean region are cold-sensitive but relatively drought resistant. The 1.35 Ma Tenaghi Phillippon pollen record in northeast Greece records a major shift towards greater aridity during interglacial periods at ~650 ka (Tzedakis et al., 2006). They suggest that continental vegetation change was independent of high-latitude glacial-interglacial marine and ice sheet records and that changes may have been a direct result of a climate change (Tzedakis et al., 2006).

Lake Van sits to the north of the orographic barrier created by the Bitlis Massif at >1600 m asl in the Eastern Anatolian high plateau region (Litt et al., 2014). The pollen record of the interglacial periods over the last 600 ka record an increase in abundance of pine (more cold-resistant) over oak (thermophilous) species. Like the Tenaghi Phillippon pollen record, the Lake Van record does not coincide perfectly with global marine and ice sheet climate records, particularly around the mid-Brunhes event (~430 ka) and marine isotope excursion 7 (250 ka), thus suggesting that obliquity/eccentricity/processional climate mechanisms may cause different responses within continental interiors (Litt et al., 2014). However, a general cooling and aridification trend is recognised, broadly consistent with global climate data in the past million year (Zachos et al., 2001; Lisiecki and Raymo, 2005).

7 Conclusions

Fe-O from the weathering profile of the Attepe iron deposits in the Eastern Taurides in southern Turkey yield He loss-corrected (U-Th)/He ages of between 5.18 and 0.95 Ma. In the three mines where two samples were analysed He ages decrease with elevation, typical of a lowering water table. This is consistent with river incision and rock uplift rates of between 12.3 to 6.4 m/Myr between 5 and 1 Ma across the region. This suggests that the region was already at or close to its current elevation by the late Miocene. Uplift/incision rates are closer to climate-induced uplift/incision recorded within the CAP over the past 2 Ma. The presence of supergene iron oxy-hydroxides throughout the ore deposits of the Attepe region suggest that the Plio-Pleistocene climate at the time was hotter and more humid than today. The latest goethite precipitation (0.95 Ma) constrains the onset of aridification across the region to sometime in the last million years. The clear evidence for regional and global cooling implies that changing climate rather than surface uplift was the main driver of aridification.

Acknowledgments

Data Availability Statement: we fully intend to place all data in a FAIR-compliant repository prior to publication of this manuscript.

Peter Chung, Marli de Jongh, Dr. Claire Wilson, Dr. Luigia de Nicola, and Dr. Valerie Olive are thanked for their assistance with SEM, XRD, He and ICP-MS analysis. We are grateful to Dr.

Domokos Gyore and Dr. Marta Zurakowska for day-to-day discussion and practical assistance with laboratory matters. Dr. John Faithfull is thanked for discussions regarding mineralogy. Prof. Taner Ünlü is thanked for continued support in all aspects related to Turkish geology. We are also grateful to MTA (project number: 2008-32-13-02.a) for supporting part of this study. No financial or otherwise conflicts of interest are recognised.

References

Alçiçek, H. & Alçiçek, M.C., (2014). Palustrine carbonates and pedogenic calcretes in the Çal basin of SW Anatolia: Implications for the Plio-Pleistocene regional climatic pattern in the eastern Mediterranean. *Catena*, *112*, 48-55.

Allard, T., Gautheron, C., Riffel, S. B., Balan, E., Soares, B. F., Pinna-Jamme, R., Derycke, A., Morin, G., Bueno, G. T. & Do Nascimento, N. (2018), Combined dating of goethites and kaolinites from ferruginous duricrusts. deciphering the late Neogene erosion history of Central Amazonia, *Chemical Geology*, 479, 136–150.

Allmendinger, R. W., Jordan, T. E., Kay, S. M. & Isacks, B. L. (1997), The evolution of the Altiplano-Puna plateau of the Central Andes, *Annual Review of Earth and Planetary Sciences*, 25(1), 139–174.

Beauvais, A., Bonnet, N.J., Chardon, D., Arnaud, N. and Jayananda, A. (2016). Very long term stability of passive margin escarpment constrained by ^{40}Ar/^{39}Ar dating of K-Mn oxides. *Geology*, 44, 299-302.

Bozkurt, E., (2000), Timing of extension on the Büyük Menderes Graben, western Turkey, and its tectonic implications. *Geological Society, London, Special Publications*, 173(1), 385-403.

Bozkurt, E. (2001), Neotectonics of Turkey–a synthesis, *Geodinamica acta*, 14(1-3), 3–30.

Çiner, A., Doğan, U., Yıldırım, C., Akçar, N., Ivy-Ochs, S., Alfimov, V., Kubik, P. W. & Schlüchter, C. (2015), Quaternary uplift rates of the Central Anatolian Plateau, Turkey: insights from cosmogenic isochron-burial nuclide dating of the Kızılırmak river terraces, *Quaternary Science Reviews*, 107, 81–97.

Cooper, F., Adams, B., Blundy, J., Farley, K., McKeon, R. & Ruggiero, A. (2016), Aridity induced Miocene canyon incision in the Central Andes, *Geology*, 44(8), 675–678.

Cosentino, D., Schildgen, T. F., Cipollari, P., Faranda, C., Gliozzi, E., Hudáčková, N., Lucifora, S. & Strecker, M. R. (2012), Late Miocene surface uplift of the southern margin of the Central Anatolian Plateau, central Taurides, Turkey, *GSA Bulletin* 124(1-2), 133–145.

Danisik, M., Evans, N.J., Ramanaidou, E., McDonald, B.J., Mayers, C., McInnes, B.I.A. (2013). (U–Th)/He chronology of the Robe River channel iron deposits, Hammersley Province, Western Australia. *Chemical Geology* 354, 150-162.

Deng, X.-D., Li, J.-W. & Shuster, D. L. (2017), Late Mio-Pliocene chemical weathering of the Yulong porphyry Cu deposit in the eastern Tibetan Plateau constrained by goethite (U–Th)/He dating: Implication for Asian summer monsoon, *Earth and Planetary Science Letters* 472, 289–298.

Dilek, Y. & Sandvol, E., (2009). Seismic structure, crustal architecture and tectonic evolution of the Anatolian-African plate boundary and the Cenozoic orogenic belts in the Eastern Mediterranean region. *Geological Society, London, Special Publications*, *327*(1), pp.127-160.

Doğan, U., (2011). Climate-controlled river terrace formation in the Kızılırmak Valley, Cappadocia section, Turkey: inferred from Ar–Ar dating of Quaternary basalts and terraces stratigraphy. *Geomorphology*, *126*(1-2), 66-81.

dos Santos Albuquerque, M.F., Horbe, A.M.C. & Danišík, M., (2020). Episodic weathering in Southwestern Amazonia based on (U-Th)/He dating of Fe and Mn lateritic duricrust. *Chemical Geology*, *553*, 119792.

Ehlers, T. A. & Poulsen, C. J. (2009), Influence of Andean uplift on climate and paleoaltimetry estimates, *Earth and Planetary Science Letters,* 281(3-4), 238–248.

Eren, M., Kadir, S., Hatipoglu, Z. and Gül, M., (2008). Quaternary calcrete development in the Mersin area, southern Turkey. *Turkish Journal of Earth Sciences*, *17*(4), pp.763-784.

Farley, K. (2018), Helium diffusion parameters of hematite from a single-diffusion-domain crystal, *Geochimica et Cosmochimica Acta*, 231, 117–129.

Foeken, J. P., Stuart, F. M., Dobson, K. J., Persano, C. & Vilbert, D. (2006), A diode laser system for heating minerals for (U-Th)/He chronometry, *Geochemistry, Geophysics, Geosystems*, 7(4).

Hatzfeld, D. & Molnar, P. (2010), Comparisons of the kinematics and deep structures of the Zagros and Himalaya and of the Iranian and Tibetan plateaus and geodynamic implications, *Reviews of Geophysics* 48(2).

Heim, J. A., Vasconcelos, P. M., Shuster, D. L., Farley, K. A. & Broadbent, G. (2006), Dating paleochannel iron ore by (U-Th)/He analysis of supergene goethite, Hamersley province, Australia, *Geology,* 34(3), 173–176.

Hofmann, F., Treffkorn, J. & Farley, K. A. (2020), U-loss associated with laser-heating of hematite and goethite in vacuum during (U–Th)/He dating and prevention using high O_2 partial pressure, *Chemical Geology,* 532, 119350

Jaffey, N. & Robertson, A.H., (2001). New sedimentological and structural data from the Ecemiş Fault Zone, southern Turkey: implications for its timing and offset and the Cenozoic tectonic escape of Anatolia. *Journal of the Geological Society*, *158*(2), 367-378.

Jaffey, N. & Robertson, A. (2005), Non-marine sedimentation associated with Oligocene-recent exhumation and uplift of the central Taurus mountains, S Turkey, *Sedimentary Geology,* 173(1-4), 53–89.

Kaplan, M.Y., Eren, M., Kadir, S. & Kapur, S., (2013). Mineralogical, geochemical and isotopic characteristics of Quaternary calcretes in the Adana region, southern Turkey: Implications on their origin. *Catena*, *101*, pp.164-177.

Kapur, S., Yaman, S., Go, S.L. & Yetis, C., (1993). Soil stratigraphy and Quaternary caliche in the Misis area of the Adana Basin, southern Turkey. *Catena*, *20*(5), 431-445.

Kayseri-Özer, M. S. (2017), Cenozoic vegetation and climate change in Anatolia—a study based on the IPR-vegetation analysis, *Palaeogeography, Palaeoclimatology, Palaeoecology* 467, 37–68.

Keskin, S. (2016), Attepe Demir Yatağı (Mansurlu Havzası, Adana) ve Çevresi Demir Yatakları ve Zuhurlarının Jeolojisi, Yapısal Özellikleri ve Tektoniği, PhD Thesis, Ankara Üniversitesi Fen Bilimleri Enstitüsü Doktora Tezi, 218 s., Ankara (yayınlanmamış).

Keskin, S**.,** & Ünlü, T. (2016) Attepe Bölgesindeki Siderit Oluşumlarının Mineralojik Özellikleri ve Jeotektonik Ortamı (Kayseri-Adana Havzası, Türkiye). *Hacettepe Üniversitesi, Yerbilimleri Dergisi*,. 37 (2), 93-120.

Ketcham, R.A. (2005), Forward and inverse modelling of low-temperature thermochronometry data, *Reviews in Mineralogy and Geochemistry* 58(1), 275–314.

Küpeli, Ş. (2010), Trace and rare-earth element behaviors during alteration and mineralization in the Attepe iron deposits (Feke-Adana, southern Turkey), *Journal of Geochemical Exploration,* 105(3), 51–74.

Küpeli, Ş., Karadagˇ, M. M., Ayhan, A., Döyen, A. & Arık, F. (2007), C, O, S and Sr isotope studies on the genesis of Fe-carbonate and barite mineralizations in the Attepe iron district (Adana, southern Turkey), *Geochemistry,* 67(4), 313–322.

Lee, M.R., Lindgren, P. & Sofe, M.R., (2014), Aragonite, breunnerite, calcite and dolomite in the CM carbonaceous chondrites: High fidelity recorders of progressive parent body aqueous alteration. *Geochimica et Cosmochimica Acta*, *144*, 126-156.

Lisiecki, L.E. & Raymo, M.E., (2005), A Pliocene-Pleistocene stack of 57 globally distributed benthic δ18O records. *Paleoceanography,* 20(1).

Litt, T., Pickarski, N., Heumann, G., Stockhecke, M. & Tzedakis, P.C., (2014), A 600,000 year long continental pollen record from Lake Van, eastern Anatolia (Turkey). *Quaternary Science Reviews*, *104*, 30-41.

Lüdecke, T., Mikes, T., Rojay, F. B., Cosca, M. A. & Mulch, A. (2013), Stable isotope-based reconstruction of Oligo-Miocene paleoenvironment and paleohydrology of central Anatolian lake basins (Turkey), *Turkish Journal of Earth Sciences*, 22(5), 793–819.

Meesters, A. & Dunai, T. (2005), A noniterative solution of the (U-Th)/He age equation, *Geochemistry, Geophysics, Geosystem,s* 6(4).

Meijers, M. J., Brocard, G. Y., Cosca, M. A., Lüdecke, T., Teyssier, C., Whitney, D. L. & Mulch, A. (2018), Rapid late Miocene surface uplift of the central Anatolian plateau margin, *Earth and Planetary Science Letters*, 497, 29–41.

Meijers, M. J., Brocard, G. Y., Whitney, D. L. & Mulch, A. (2020), Paleoenvironmental conditions and drainage evolution of the Central Anatolian lake system (Turkey) during late Miocene to Pliocene surface uplift, *Geosphere*, 16(2), 490–509.

Meijers, M. J., Strauss, B. E., Özkaptan, M., Feinberg, J. M., Mulch, A., Whitney, D. L. & Kaymakçı, N. (2016), Age and paleoenvironmental reconstruction of partially remagnetized lacustrine sedimentary rocks (Oligocene Aktoprak basin, central Anatolia, Turkey), *Geochemistry, Geophysics, Geosystems*, 17(3), 914–939.

Molnar, P. (2005), Mio-Pliocene growth of the Tibetan plateau and evolution of east Asian climate, *Palaeontologia Electronica*, 8(1), 1–23.

Molnar, P., England, P. & Martinod, J. (1993), Mantle dynamics, uplift of the Tibetan plateau, and the Indian monsoon, *Reviews of Geophysics*, 31(4), 357–396.

Monteiro, H. S., Vasconcelos, P. M., Farley, K. A., Spier, C. A. & Mello, C. L. (2014), (U–Th)/He geochronology of goethite and the origin and evolution of Cangas, *Geochimica et Cosmochimica Acta*, 131, 267–289.

Ocakoğlu, F. (2002), Palaeoenvironmental analysis of a Miocene basin in the high Taurus mountains (southern Turkey) and its palaeogeographical and structural significance, *Geological Magazine*, 139(4), 473–487.

Öğretmen, N., Cipollari, P., Frezza, V., Faranda, C., Karanika, K., Gliozzi, E., Radeff, G. & Cosentino, D. (2018), Evidence for 1.5 km of uplift of the Central Anatolian plateau's southern margin in the last 450 kyr and implications for its multiphased uplift history, *Tectonics* 37(1), 359–390.

Parlak, O., Karaoğlan, F., Rızaoğlu, T., Klötzli, U., Koller, F. & Billor, Z. (2013), U–Pb and ^{40}Ar–^{39}Ar geochronology of the ophiolites and granitoids from the Tauride belt: Implications for the evolution of the inner Tauride suture, *Journal of Geodynamics*, 65, 22–39

Racano, S., Jara-Muñoz, J., Cosentino, D. & Melnick, D. (2020), Variable quaternary uplift along the southern margin of the Central Anatolian plateau inferred from modelling marine terrace sequences, *Tectonics*, **https://doi.org/10.1029/2019TC005921**

Radeff, G. (2014), Geohistory of the Central Anatolian plateau southern margin (southern Turkey). PhD thesis, Potsdam University.

Robertson, A. & Grasso, M. (1995), Overview of the late Tertiary–recent tectonic and palaeo environmental development of the Mediterranean region, *Terra Nova*, 7(2), 114–127.

Ryan, W.B., Carbotte, S.M., Coplan, J.O., O'Hara, S., Melkonian, A., Arko, R., Weissel, R.A., Ferrini, V., Goodwillie, A., Nitsche, F. and Bonczkowski, J., (2009). Global multi-resolution topography synthesis. *Geochemistry, Geophysics, Geosystems*, *10*(3).

Sarıkaya, M.A., Yıldırım, C. & Çiner, A., (2015), Late Quaternary alluvial fans of Emli Valley in the Ecemiş Fault Zone, south central Turkey: Insights from cosmogenic nuclides. *Geomorphology*, *228*, pp.512-525.

Schemmel, F., Mikes, T., Rojay, B. & Mulch, A. (2013), The impact of topography on isotopes in precipitation across the Central Anatolian plateau (Turkey), *American Journal of Science,* 313(2), 61–80.

Schildgen, T.F., Cosentino, D., Bookhagen, B., Niedermann, S., Yıldırım, C., Echtler, H., Wittmann, H. & Strecker, M. R. (2012), Multi-phased uplift of the southern margin of the Central Anatolian plateau, Turkey: A record of tectonic and upper mantle processes, *Earth and Planetary Science Letters*, 317, 85–95.

Schildgen, T.F., Yıldırım, C., Cosentino, D. & Strecker, M. R. (2014), Linking slab break-off, Hellenic trench retreat, and uplift of the Central and Eastern Anatolian plateaus, *Earth Science Reviews*, 128, 147–168.

Şengör, A., Görür, N. & Şaroğlu, F. (1985), Strike-slip faulting and related basin formation in zones of tectonic escape: Turkey as a case study. in Strike-Slip Faulting and Basin Formation, edited by Biddle, K.T., & Christie-Blick, N. *Special publication - Society of Economic Paleontologists and Mineralogists*, 37, 227-264.

Sensoy, S. (2004), The mountains influence on Turkey climate, *in* Balwois Conference on Water Observation and Information System for Decision Support.

Shuster, D. L., Vasconcelos, P. M., Heim, J. A. & Farley, K. A. (2005), Weathering geochronology by (U-Th)/He dating of goethite, *Geochimica et Cosmochimica Acta*, 69(3), 659–673.

Svenning, J.C., (2003), Deterministic Plio-Pleistocene extinctions in the European cool-temperate tree flora. *Ecology Letters*, 6(7), 646-653.

Tardy, Y. and Nahon, D., (1985), Geochemistry of laterites, stability of Al-goethite, Al-hematite, and Fe^{3+}-kaolinite in bauxites and ferricretes: an approach to the mechanism of concretion formation. *American Journal of Science*, *285*(10), 865-903.

Taylor, R. (2011), Boxworks and related features, *in* Gossans and Leached Cappings, Springer, 77–106.

Tzedakis, P.C., Hooghiemstra, H. & Pälike, H., (2006), The last 1.35 million years at Tenaghi Philippon: revised chronostratigraphy and long-term vegetation trends. *Quaternary Science Reviews*, *25*(23-24), 3416-3430.

Vasconcelos, P.-M. (1999), K-Ar and $^{40}Ar/^{39}Ar$ geochronology of weathering processes, *Annual Review of Earth and Planetary Sciences*, 27(1), 183–229.

Vasconcelos, P.-M., Heim, J. A., Farley, K. A., Monteiro, H. & Waltenberg, K. (2013), $^{40}Ar/^{39}Ar$ and (U–Th)/He–$^{4}He/^{3}He$ geochronology of landscape evolution and channel iron deposit genesis at Lynn Peak, Western Australia, *Geochimica et Cosmochimica Acta*, 117, 283–312.

Vasconcelos, P.-M., Reich, M. & Shuster, D. L. (2015), The paleoclimatic signatures of supergene metal deposits, *Elements*, 11(5), 317–322.

Walsh-Kennedy, S., Aksu, A.E., Hall, J., Hiscott, R.N., Yaltırak, C. & Çifçi, G., 2014. Source to sink: The development of the latest Messinian to Pliocene–Quaternary Cilicia and Adana Basins and their linkages with the onland Mut Basin, eastern Mediterranean. *Tectonophysics*, *622*, 1-21.

Wu, L.-Y., Stuart, F. M., Di Nicola, L., Heizler, M., Benvenuti, M. & Hu, R.-Z. (2019), Multi-aliquot method for determining (U+ Th)/He ages of hydrothermal hematite: Returning to Elba, *Chemical Geology*, 504, 151–157.

Yıldırım, C., Sarıkaya, M. A. & Çiner, A. (2016), Late Pleistocene intraplate extension of the central Anatolian plateau, Turkey: Inferences from cosmogenic exposure dating of alluvial fan, landslide, and moraine surfaces along the Ecemiş fault zone, *Tectonics* 35(6), 1446– 1464.

Zachos, J., Pagani, M., Sloan, L., Thomas, E. & Billups, K. (2001), Trends, rhythms, and aberrations in global climate 65 Ma to present, S*cience*, 292(5517), 686–693.

AGU PUBLICATIONS

Tectonics

Supporting Information for

Early Pleistocene aridification of the Eastern Taurides, Turkey revealed by (U-Th)/He ages of supergene Attepe iron deposits

D. Currie[1], S. Keskin[2], and F. M. Stuart[1]

[1] Isotope Geosciences, Scottish Universities Environmental Research Centre, Rankine Avenue, East Kilbride G75 0QF, UK.

[2] General Directorate of Mineral Research and Exploration, Eastern Black Sea District Office, Trabzon, Turkey.

Contents of this file

Introduction

Supporting information provided allows the reader further insight into where samples were collected from in relation to Earth's surface and what these samples look like in hand sample (Figures S1-S5). Following this, a general guide to each geological formation and their relation to ore mineralisation is provided in a stratigraphic column whilst cross sections are provided to give a sense of scale of each ore deposit (Figures S6-S7). To back up finer mineralogical insight discussed in the main text, diffractograms used to determine mineral phases present in each sample are given (Figure S8) as well as data gathered from the same analysis then processed to calculate crystallite size of each sample using the Scherrer equation (Table S1). Finally, plots of sample age against eU, crystallite size, and mineralogy are provided to back up suggestion in main text that no relationship between these aspects was noted (Figures S9-S10).

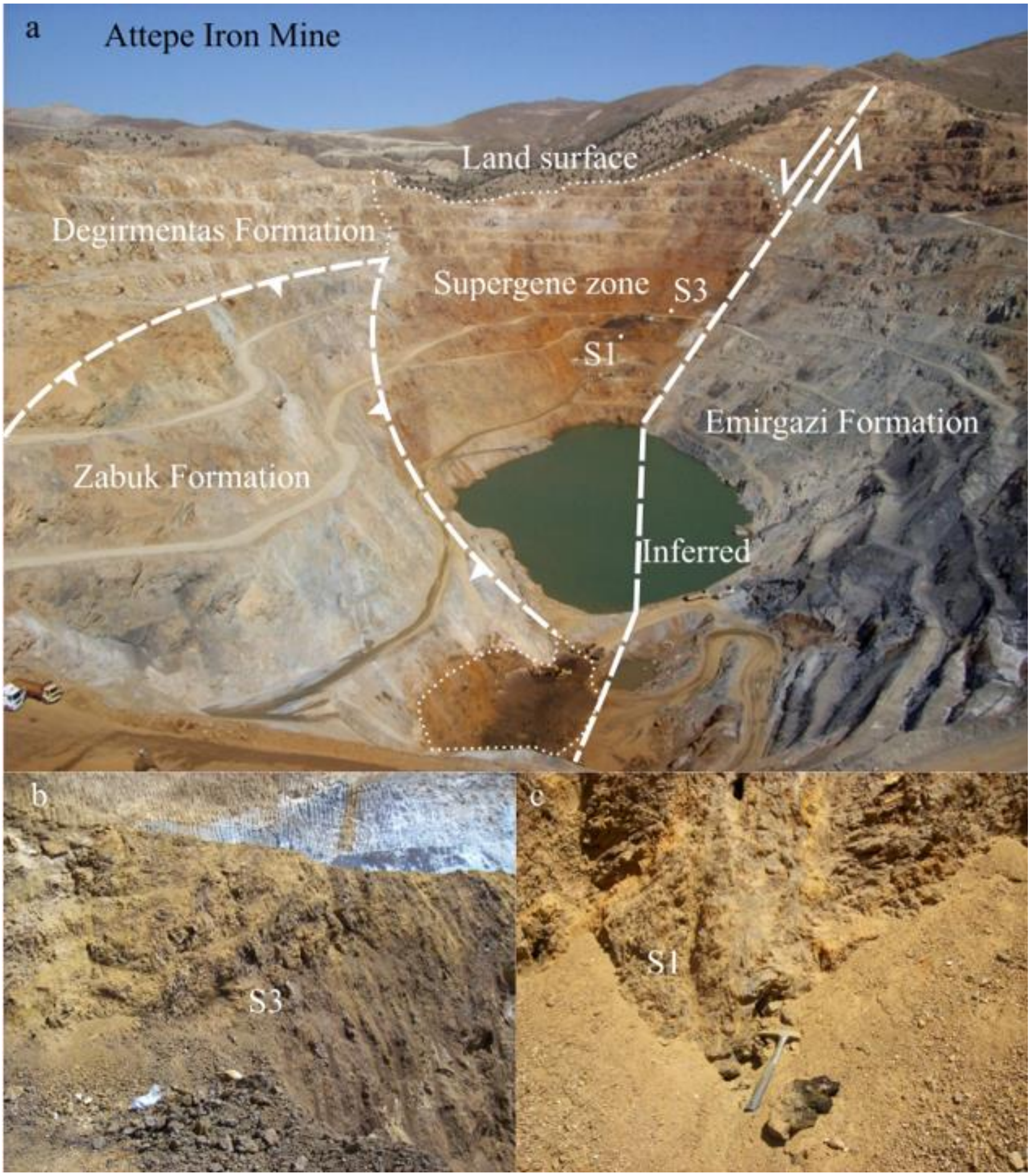

Figure S1. Field images of Attepe iron mine. A) view of the open pit mine. B) location of sample S1. C) location of sample S3.

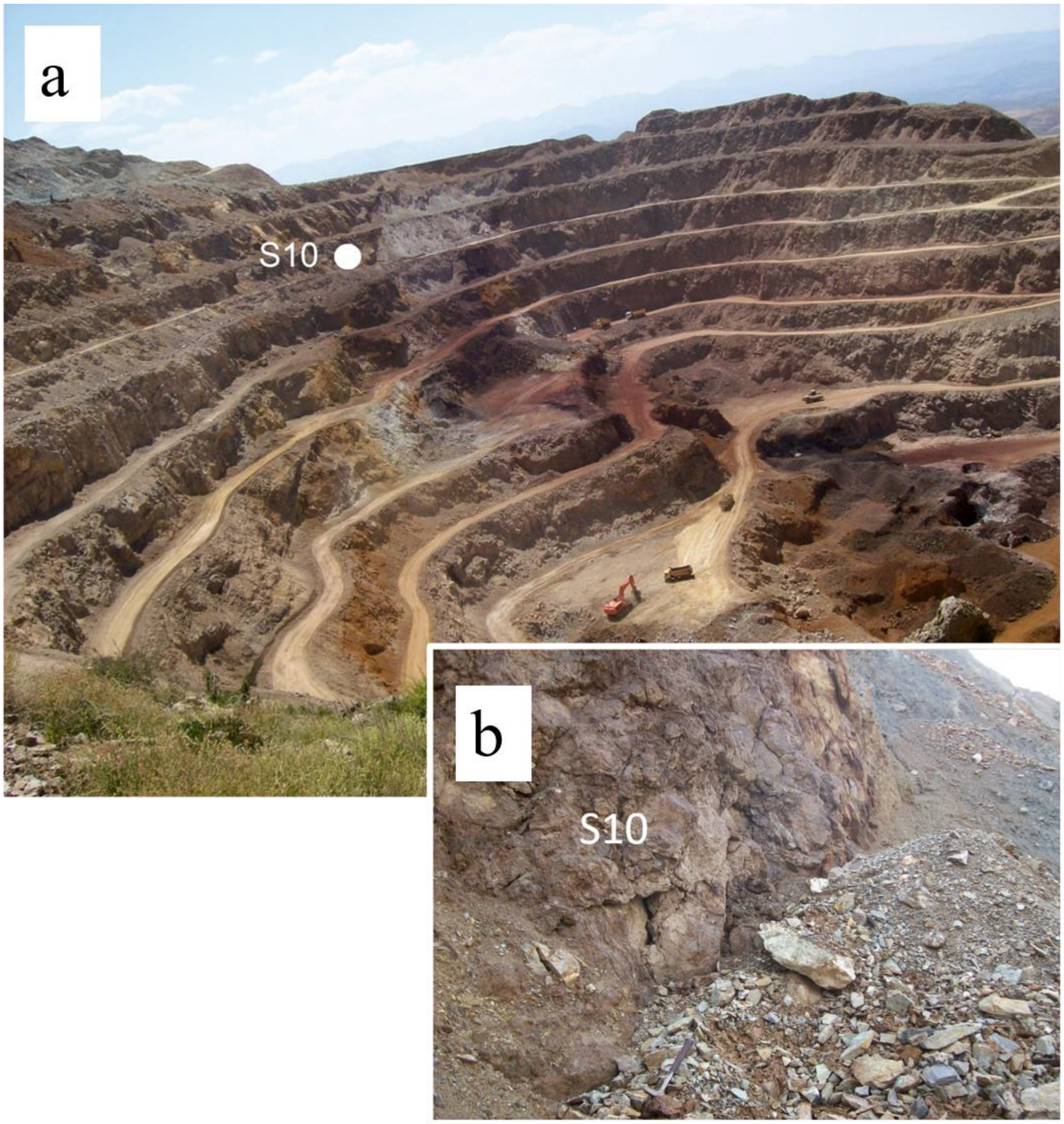

Figure S2. Field images of Karacat iron mine A) and B) the location of sample S10.

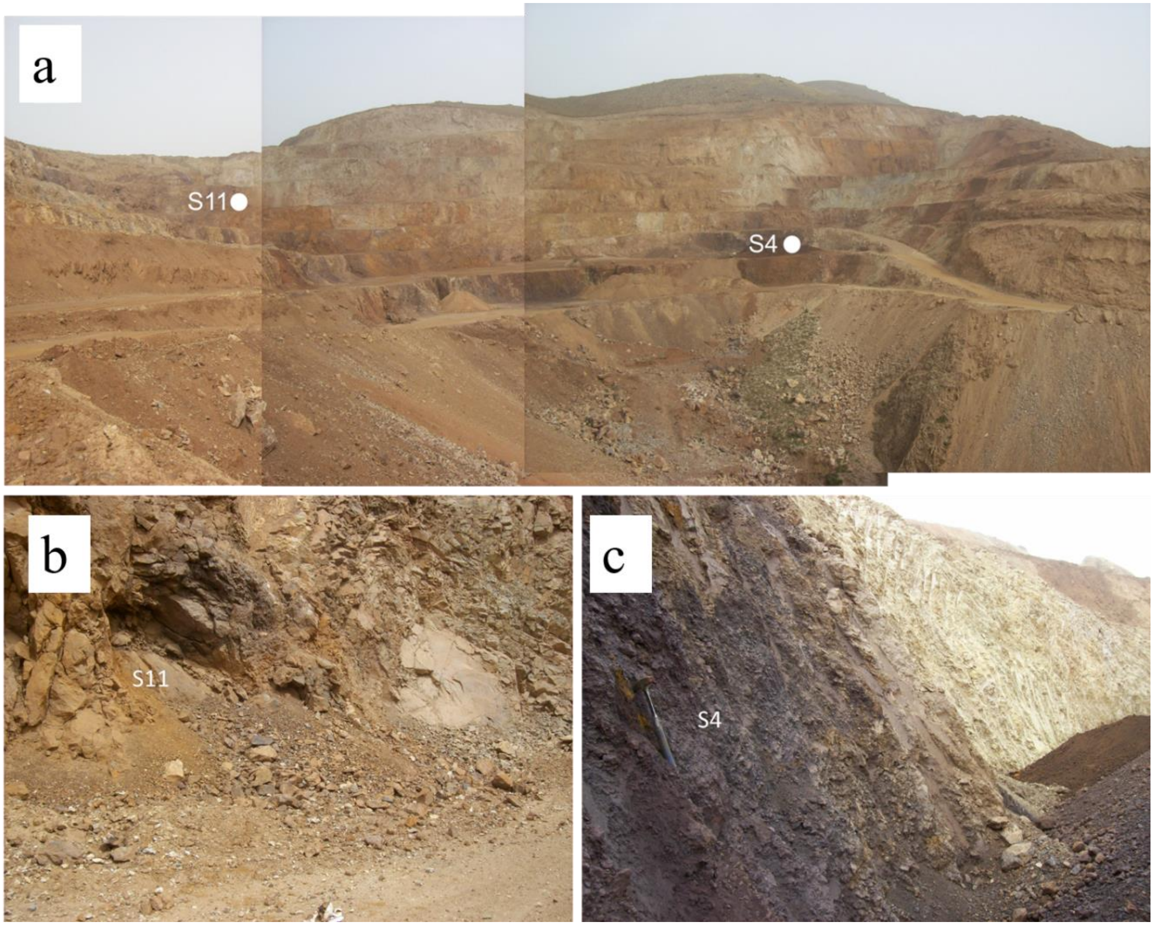

Figure S3. Field images of Elmadagbeli iron mine showing the open pit mine A) and the location of samples S11 (B) and S4 (C).

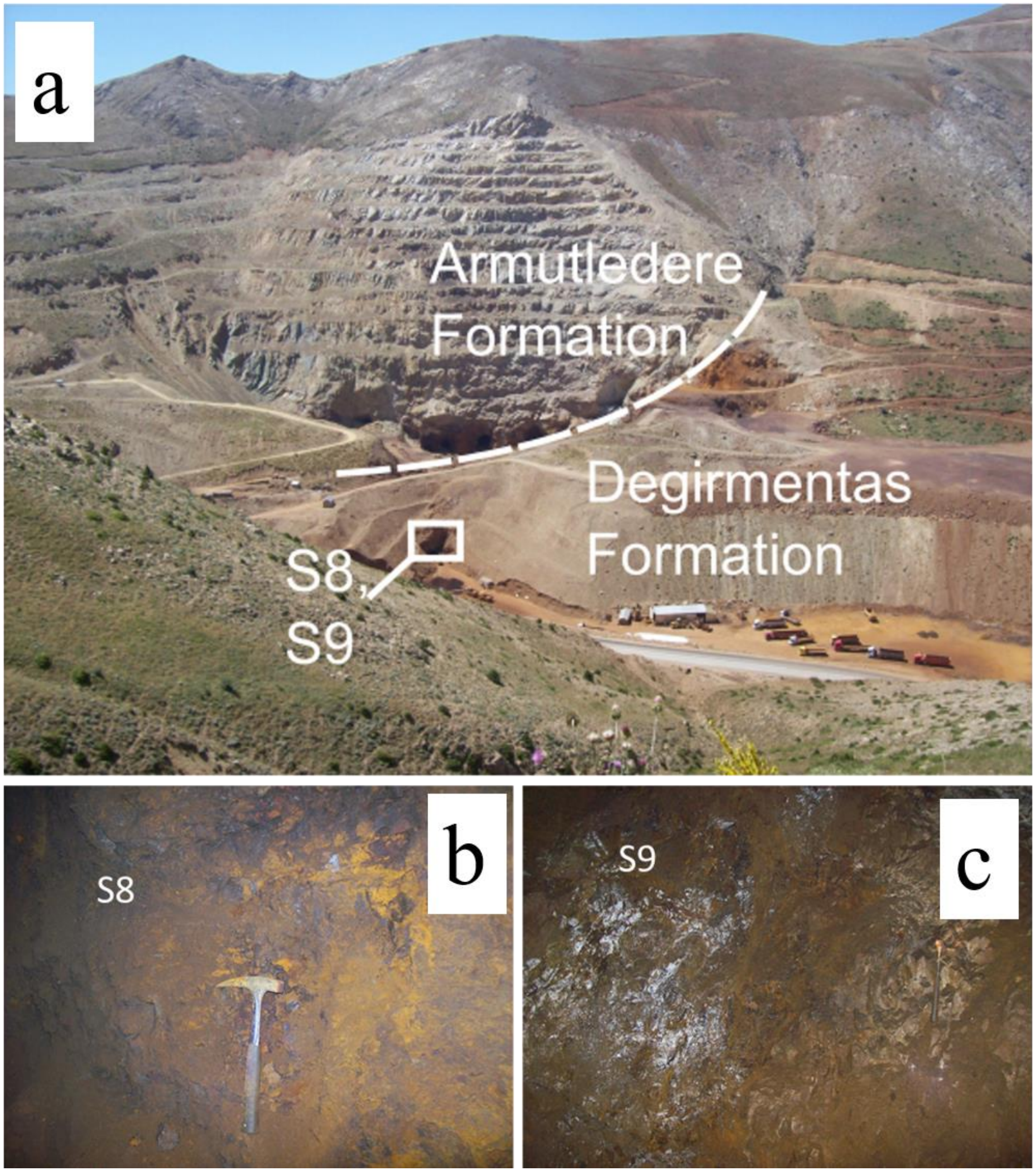

Figure S4. Photograph of the Magarabeli iron mine (A). Samples were taken from section of the mine highlighted within the white box in image A. B) context of sample S8. C) context of sample S9.

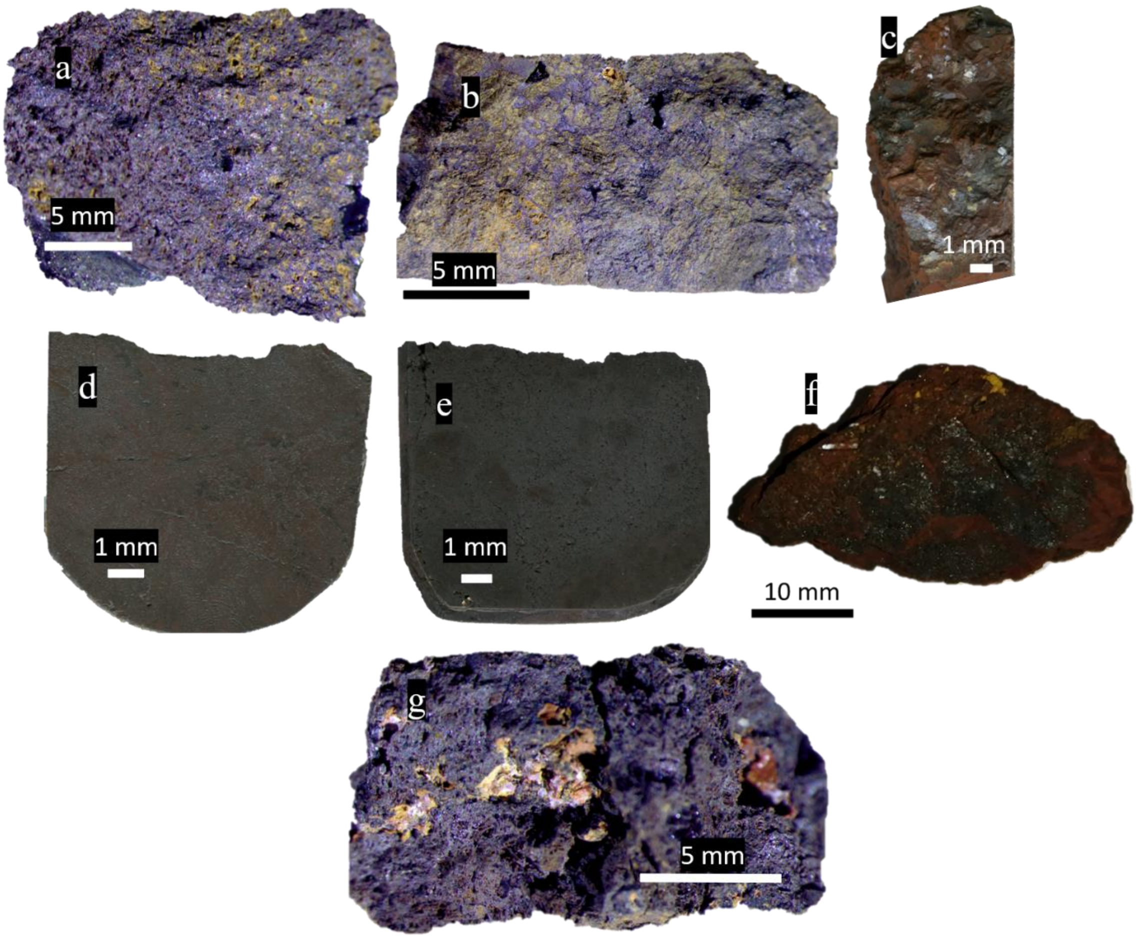

Figure S5. Images of hand samples used in this study. A) Sample S1: fresh surface of a chip liberated from larger sample. Metallic grey of goethite with friable yellow weathering evident. B) Sample S3: fresh surface of a chip liberated from larger sample. Metallic grey of goethite with friable yellow weathering evident. C) Sample S4: Representative broken chip, similar to that used for SEM analysis, showing fresher metallic grey of hematite and deeper red weathering. D) Sample S8: Broken polished block showing metallic lustre of hematite and weathered hematite/goethite red/brown patchy surface. E) Sample S9: Broken polished block showing metallic lustre of hematite/magnetitie and weathered red patchy surface. F) Sample S10: Broken chip showing darker metallic lustre of hematite alongside friable weathered red and yellow patches. G) Sample S11: fresh surface of a chip liberated from larger sample. Metallic grey of goethite with friable yellow weathering evident.

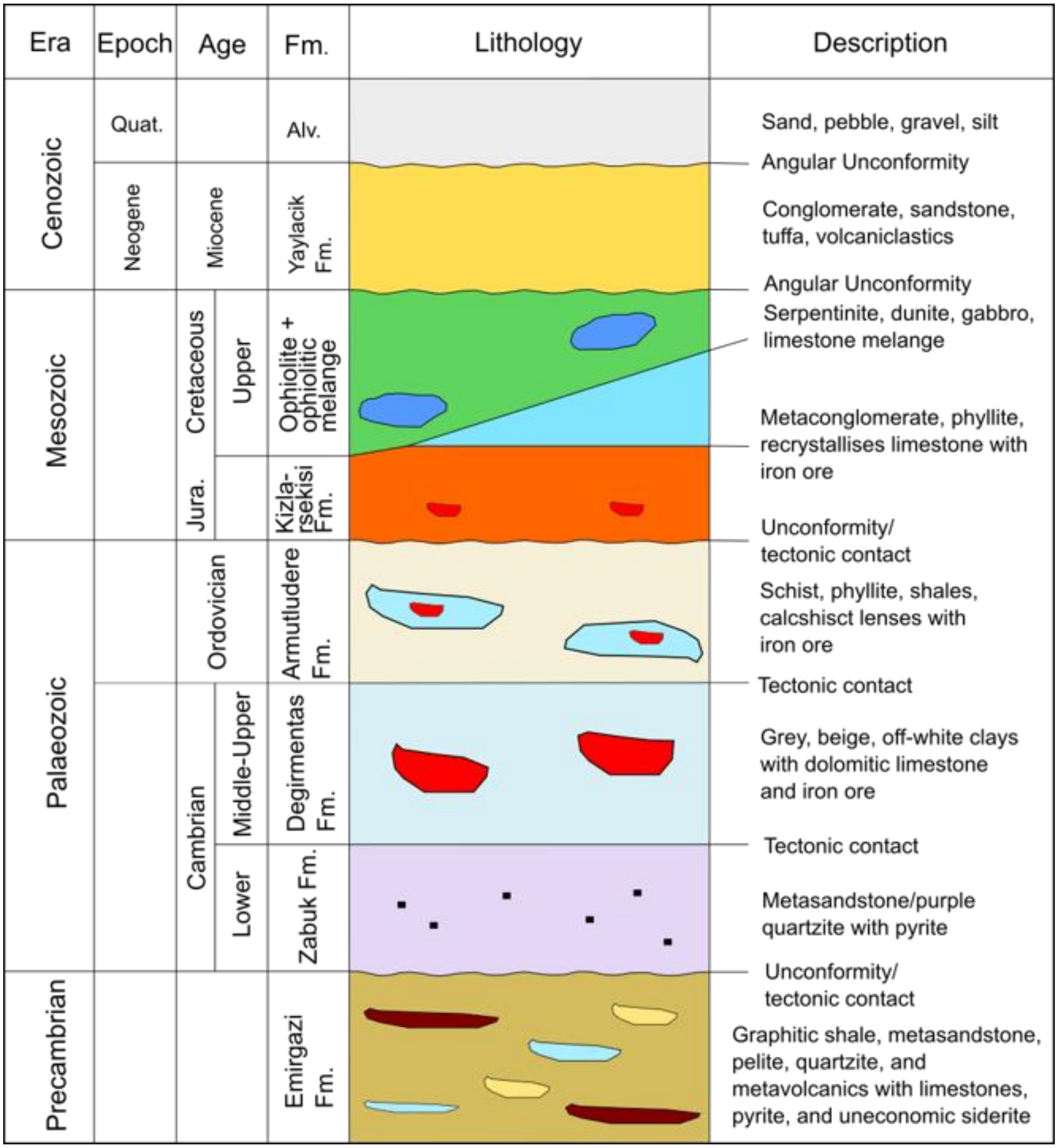

Figure S6. Stratigraphic column showing the main geological units across the Attepe ore deposit region. Adapted from Keskin (2016)

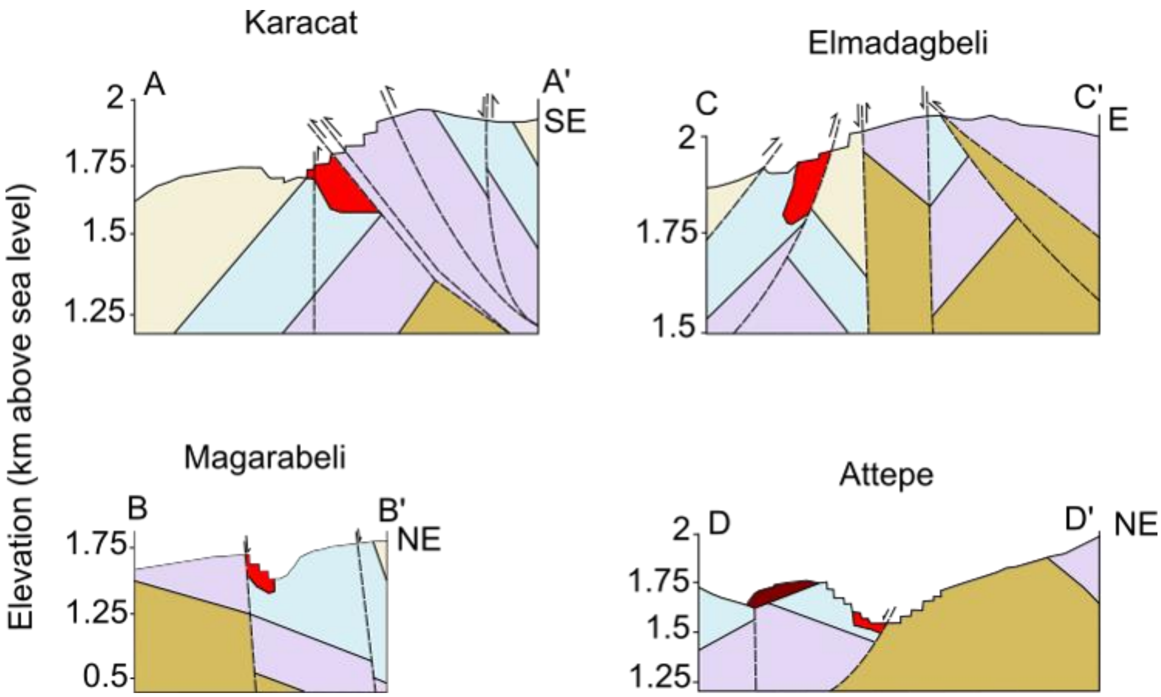

Figure S7. Cross sections of each mine showing relationship to main lithologies and faults. Cross section lines are taken from Fig. 1. C in main text. Adapted from Keskin (2016)

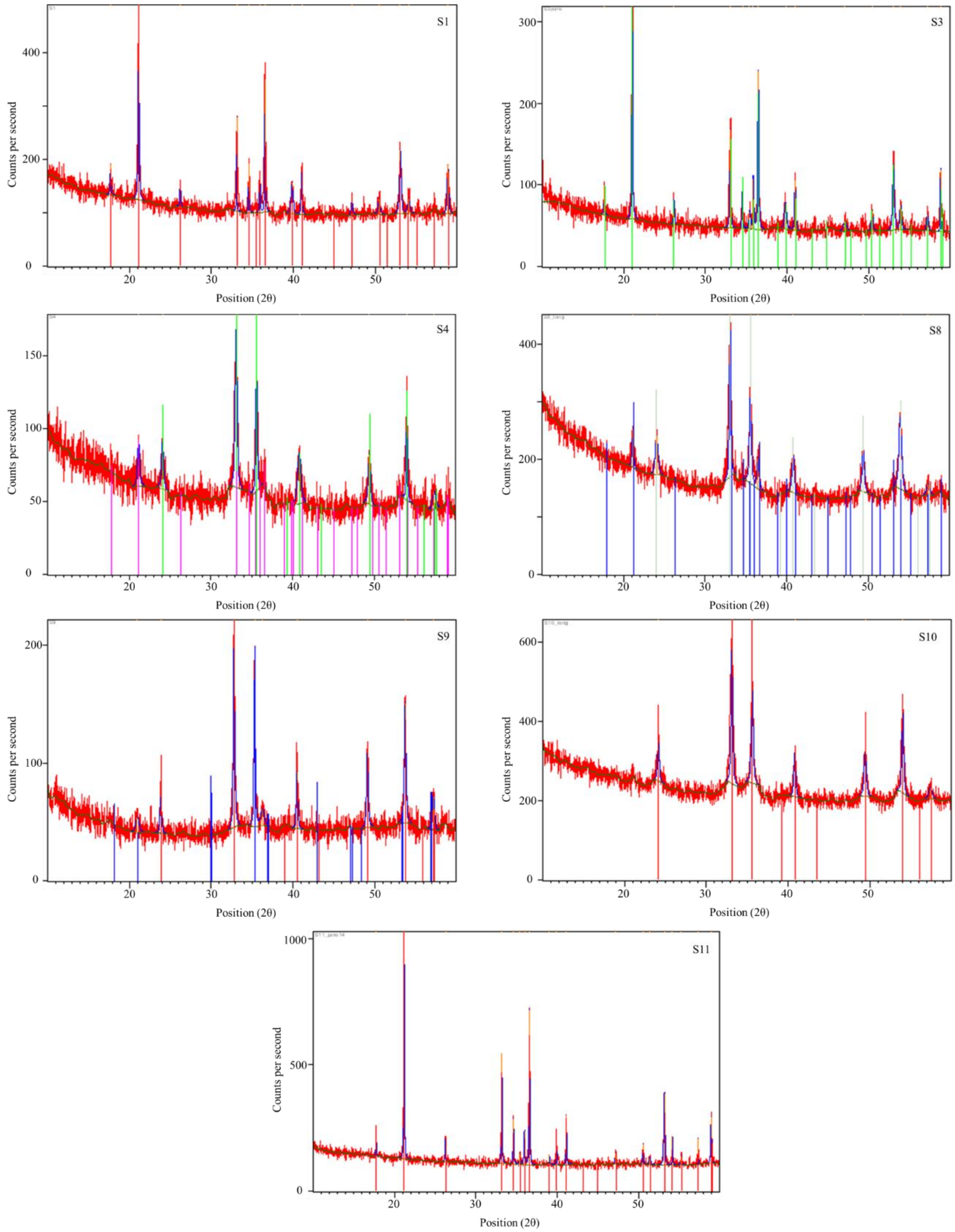

Figure S8. Diffractograms of each sample. S1: Highest intensity peak recorded at 21.1θ indicative of goethite. S3: Highest intensity peak recorded at 21θ indicative of goethite. S4: Highest intensity peak recorded at 31.1θ indicative of hematite, with goethite a minor component recording 63 % and 32 % relative peak height (violet lines under diffractogram) and < 20 nm crystallite size. S8: Highest intensity peak recorded at 31.1θ indicative of hematite, with goethite a minor component recording a 52 % relative peak height (blue lines45 under diffractogram) and 22 nm crystallite size. S9: Highest intensity peak recorded at 32.8θ indicative of hematite, with magnetite recording a 78 % relative peak height at 35.3θ (blue lines under diffractogram). S10: Highest intensity peak recorded at 31.1θ indicative of hematite. S11: Highest intensity peak recorded at 21.1θ indicative of goethite.

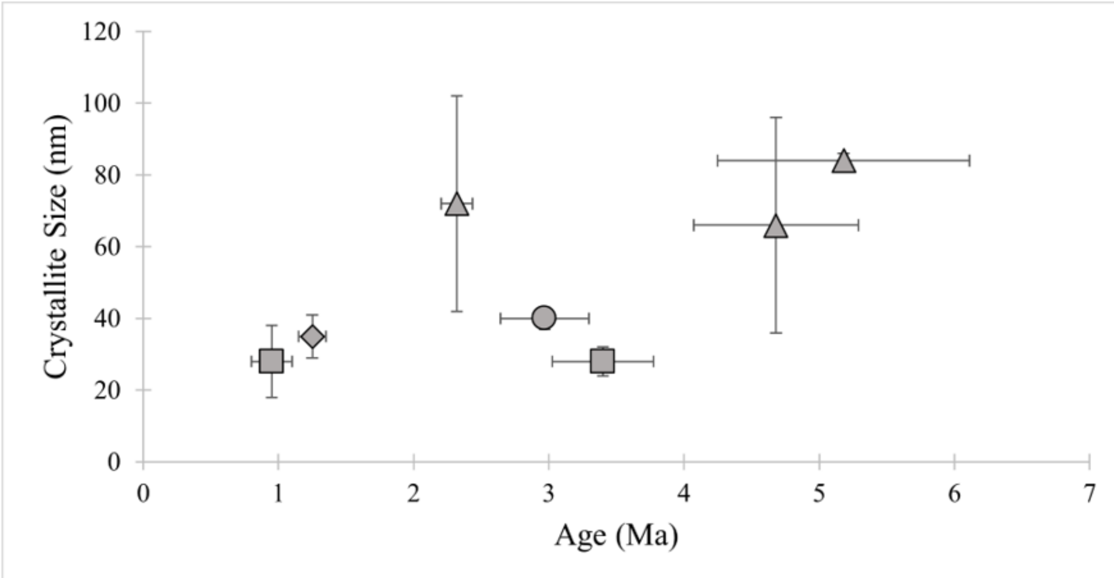

Figure S9. Age versus crystallite size and mineralogy plot. Triangle = goethite; circle = hematite/magnetite mix; square = hematite/goethite mix; rhombus = hematite

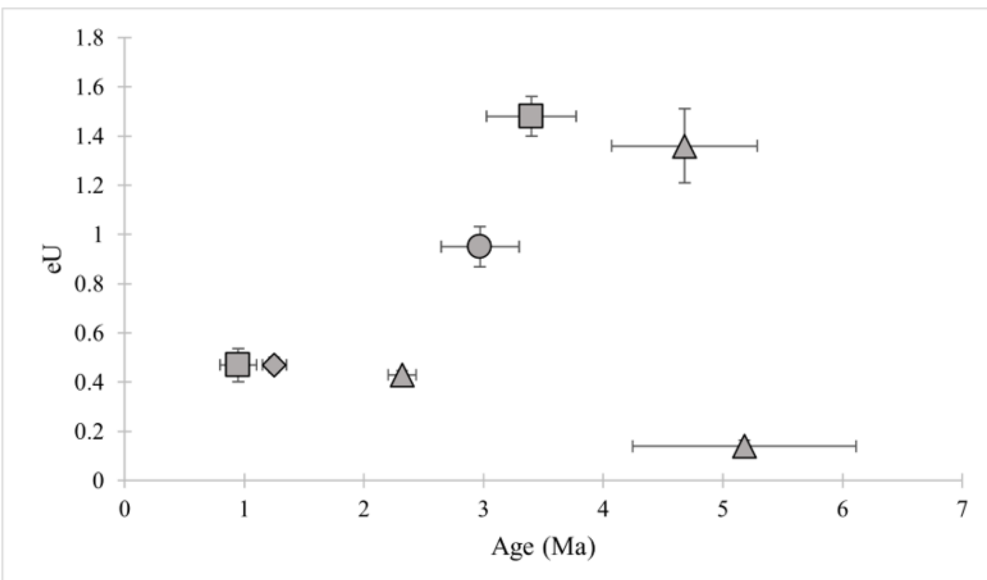

Figure S10. Age versus eU and mineralogy plot. Triangle = goethite; circle = hematite/magnetite mix; square = hematite/goethite mix; rhombus = hematite.

Sample	Mineralogy	Relative Intensity (%)	FWHM (degrees)	FWHM (radians)	Peak Position (degrees)	Peak Position (radians)	D	D average	stdev	error
S1	FeOOH	100	0.1428	0.0025	21.1	0.2	59.1	72.2	29.9	41.4%
	FeOOH	48	0.0816	0.0014	33.1	0.3	106.1			
	FeOOH	69	0.1020	0.0018	36.6	0.3	85.7			
	FeOOH	33	0.2448	0.0043	53.1	0.5	37.9			
S3	FeOOH	100	0.1428	0.0025	21.1	0.2	59.1	65.6	30.0	45.7%
	FeOOH	78	0.1632	0.0028	36.5	0.3	53.5			
	FeOOH	49	0.1428	0.0025	33.1	0.3	60.6			
	FeOOH	33	0.2448	0.0043	53.0	0.5	37.9			
	FeOOH	31	0.0816	0.0014	58.8	0.5	116.7			
S4	Fe_2O_3	100	0.2856	0.0050	33.1	0.3	30.3	27.6	10.0	36.2%
	Fe_2O_3	88	0.2040	0.0036	35.6	0.3	42.7			
	FeOOH	63	0.4896	0.0085	54.0	0.5	19.0			
	FeOOH	32	0.4896	0.0085	40.8	0.4	18.1			
	Fe_2O_3	31	0.3264	0.0057	49.4	0.4	28.0			
S8	Fe_2O_3	100	0.2856	0.0050	33.1	0.3	30.3	27.9	4.4	15.7%
	Fe_2O_3	57	0.2856	0.0050	35.6	0.3	30.5			
	FeOOH	52	0.4080	0.0071	53.9	0.5	22.8			
S9	Fe_2O_3	100	0.2040	0.0036	32.8	0.3	42.4	40.1	2.9	7.1%
	Fe_3O_4	78	0.2040	0.0036	35.3	0.3	42.7			
	Fe_2O_3	61	0.2448	0.0043	53.7	0.5	38.0			
	Fe_2O_3	38	0.2448	0.0043	49.1	0.4	37.3			
S10	Fe_2O_3	100	0.2244	0.0039	33.1	0.3	38.6	34.5	5.7	16.5%
	Fe_2O_3	61	0.2856	0.0050	35.6	0.3	30.5			
	Fe_2O_3	57	0.2448	0.0043	54.0	0.5	38.0			
S11	FeOOH	100	0.1020	0.0018	21.2	0.2	82.8	84.4	1.5	1.8%
	FeOOH	48	0.1020	0.0018	33.2	0.3	84.9			
	FeOOH	68	0.1020	0.0018	36.6	0.3	85.7			
							Average D (nm)	50.3	23.3	46.2%

Scherrer equation D = k x λ / β (cosθ)

D = crystallite size (nm)

k = Scherrer's Constant (for spherical crystallites with cubic symmetry) 0.94

λ = x-ray wavelength Cu K-alpha 1.5406; or 0.15406 Angstrom.

β = FWHM (Full Width Half Maximum in radians - peak width)

θ = peak position (radians) 0.5

Table S1. XRD diffractogram data from iron oxide/oxyhydroxide samples from the Attepe iron deposits, Turkey.